國立臺灣大學工學院材料科學與工程學系暨研究所

碩士論文

Department of Materials Science and Engineering
College of Engineering
National Taiwan University
Master's Thesis

藉由垂直磁異相性調控零場鐵磁共振頻率

Tuning the zero-field ferromagnetic resonance frequency by modifying the perpendicular magnetic anisotropy

徐沛汝

Pei-Ju Hsu

指導教授 : 白奇峰博士

Advisor : Chi-Feng Pai, Ph.D.

中華民國 113 年 7 月

July, 2024

doi:10.6342/NTU202403229

國立臺灣大學碩士學位論文
口試委員會審定書
MASTER'S THESIS ACCEPTANCE CERTIFICATE
NATIONAL TAIWAN UNIVERSITY

（論文中文題目）
(Chinese title of Master's Thesisn)

藉由垂直磁異相性調控零場鐵磁共振頻率

（論文英文題目）
(English title of Master's Thesis)

Tuning the zero-field ferromagnetic resonance frequency by modifying the perpendicular magnetic anisotropy

本論文係 **徐沛汝** (R11527051) 在國立臺灣大學材料科學與工程學系、所完成之碩士學位論文，於民國 113 年 7 月 29 日承下列考試委員審查通過及口試及格，特此證明。

The undersigned, appointed by the Department / Graduate Institute of Material Science and Engineering on 29th/July/2024 have examined a Master's Thesis entitled above presented by **Hsu, Pei-Ju** (R11527051) candidate and hereby certify that it is worthy of acceptance.

口試委員
Oral examination committee:

白奇峰 白奇峰
（指導教授 Advisor）

宋明遠 宋明遠

胡宸瑜 胡宸瑜

系（所、學位學程）主管 Director：蔡豐羽 蔡豐羽

doi:10.6342/NTU202403229

誌謝

很高興能在碩班期間加入白奇峰老師實驗室，在研究所期間學習到了很多有關磁性與自旋電子學相關領域的知識，雖然一開始我對於這個領域感到有點陌生，但非常感謝老師在研究中的悉心指導，總是非常樂意且耐心的解答我的疑惑，當研究遇到問題時，也提供了非常多的建議和方向，使我能順利完成我的研究。

非常感謝 SCREAM TEAM 的所有成員，謝謝佳晉學長在一開始進入實驗室時，總是非常耐心的協助我理解元件的製作和量測，在課業上也給予我非常多的建議和幫助。同時也謝謝博班的宇豪學長，唯邦學長和俊逸學長在量測儀器出問時，總是不吝給予協助。謝謝宸瑜學長在口試以及在論文上的建議，幫助我挑出了許多錯誤，真的非常感謝。謝謝胤君學長，智晨，子晏，哲睿，冠宇和翊文與我討論有關量測或實驗上的問題，謝謝瑞旭常常帶我量測一些我沒接觸過的儀器和灌輸我一些奇異的知識，謝謝孟頡，文翰，聖文，詠絢和書鋒的陪伴，有了你們，讓我在研究生活中不孤單也充滿了歡笑聲，很高興能認識大家。

最後感謝我的家人，在求學期間，不管在經濟上或是精神上總是給予最大的支持，做為我最強力的後盾，讓我能安心在我的課業上，也謝謝比比和憲翔，在我焦慮時總是能當我心靈上的依靠，傾聽我的煩惱。

很幸運能獲得許多人的幫助，才能使我在研究上更順利，也使我的碩士生活不枯燥並充滿歡樂，畢業後我會想念在 SCREAM TEAM 的時光，想念台大，想念大家。

doi:10.6342/NTU202403229

中文摘要

隨著無線通訊的發展，電子產品追求超高頻、高速、輕薄化以及低功耗等性能。電子裝置的操作頻率也因而不斷提高。應用在這些裝置中的集成電感在高頻的需求也因此逐漸增長。相較於非磁性集成電感，磁性集成電感可以提供較高的感值，但由於鐵芯材料的鐵損和鐵磁共振頻率的限制，在高頻應用中仍有許多挑戰。鐵磁共振頻率是決定電感工作頻率的一個重要參數，當頻率達到鐵磁共振頻率時，材料對交變磁場的能量吸收達到最大，同時電感的工作效能也因而大幅下降。因此，研發具有高鐵磁共振頻率的鐵芯材料是重要的。

在這篇論文中，我將在 Pt/Co/Pt 和 W/CoFeB/MgO 這兩種具有垂直磁異相性的膜層系統中，藉由設計膜層結構和鐵磁層厚度來調控垂直磁異相性強度，進而去調節材料的鐵磁共振頻率。我的研究分成兩部分，在第一部分，我會先在 Pt/Co/Pt 和 W/CoFeB/MgO 單層鐵磁層系統中，對鐵磁共振頻率和矯頑磁場作對鐵磁層厚度的分析，以找出最佳的厚度參數。在第二部分，我們將以最佳鐵磁層厚度參數做成 Pt/Co/Pt 和 W/CoFeB/MgO 多層鐵磁層系統，並對重複層數或結構做鐵磁共振頻率及矯頑磁場的調整。研究結果顯示，具有較強垂直磁異相性的樣品，可以使零場鐵磁共振頻率從零調至更高的頻段。總體來看，W/CoFeB/MgO 多層鐵磁層系統相較 Pt/Co/Pt 多層鐵磁層系統有較大的鐵磁共振頻率以及較低的矯頑磁場，隨著重複層數增加仍可以維持在>10GHz 的頻段，顯示了其作為高頻集成電感鐵芯材料的潛力。然而，相較於其他研究，W/CoFeB/MgO 多層膜系統的矯頑磁場仍是大上許多，且為了能在實際應用中有明顯的感值增加，在更高層數的表現仍需要被研究。因此將其實際應用在高頻磁芯材料上還有許多的改善空間。

關鍵字:高頻電感鐵芯材料、鐵磁共振頻率、垂直磁異相性、鐵磁多層膜、自旋傳輸鐵磁共振

doi:10.6342/NTU202403229

Abstract

With the advancement of wireless communication, electronic products are striving for ultra-high frequency, high speed, lightweight, and low power consumption, leading to the operating frequency of electronic devices continuing to increase. In wireless communication applications, the integrated inductor is an indispensable component in the circuits. Consequently, there is a growing demand for integrated inductors designed for exceptional high-frequency performance. In contrast to non-magnetic integrated inductors, magnetic integrated inductors possess a relatively high inductance value. However, due to the core loss and the limit of the resonance frequency of the magnetic core materials, there are also some challenges in high-frequency applications. The ferromagnetic resonance frequency is a crucial parameter that determines the operating frequency of the inductor. When the frequency reaches the ferromagnetic resonance frequency, the magnetic material absorbs the energy from the alternating magnetic field, leading to a significant decrease in inductance. Hence, it is vital to develop a core material with a high ferromagnetic resonance frequency.

In this paper, I will focus on four systems with perpendicular magnetic anisotropy, which are Pt/Co/Pt system, Pt/Co/Pt multilayer system, W/CoFeB/MgO system, and W/CoFeB/MgO multilayer system. The ferromagnetic resonance frequency and coercivity field will be investigated by modifying the PMA in these systems. The study is divided into two parts. In the first part, I will analyze the ferromagnetic resonance frequency and coercivity depending on the ferromagnetic layer thickness in Pt/Co/Pt and W/CoFeB/MgO systems to determine the optimal ferromagnetic layer thickness. In the second part, the Pt/Co/Pt multilayer system and the W/CoFeB/MgO multilayer system

doi:10.6342/NTU202403229

will be investigated with several repeats of the optimal ferromagnetic thickness. The results indicate the zero-field ferromagnetic resonance frequency (f_0) can be tilted away from 0 if a sample exhibits a sizable PMA strength. Overall, the samples in W/CoFeB/MgO multilayer system possess a higher f_0 (>14GHz) and lower coercivity field than those in the Pt/Co/Pt multilayer system. This high level of f_0 demonstrates their potential for high-frequency inductor core materials. However, the coercivity in W/CoFeB/MgO system is still considerable compared to other studies. To substantially enhance inductance in practical applications, further study on W/CoFeB/MgO multilayer systems with higher repetition of the ferromagnetic layer is needed. Therefore, it still needs lots of work to reach its full potential for the high-frequency magnetic core material.

Keywords: High-frequency inductor core materials, Ferromagnetic resonance, Perpendicular magnetic anisotropy, Magnetic multilayers, Spin-torque ferromagnetic resonance

doi:10.6342/NTU202403229

Contents

doi:10.6342/NTU202403229

doi:10.6342/NTU202403229

List of Figures

doi:10.6342/NTU202403229

doi:10.6342/NTU202403229

doi:10.6342/NTU202403229

doi:10.6342/NTU202403229

List of Tables

doi:10.6342/NTU202403229

Chapter 1 Introduction

1.1 Magnetic Anisotropy

1.1.1 Shape anisotropy

Magnetic anisotropy refers to the directional dependence of a material's magnetic properties, and it can arise due to several factors, including shape anisotropy, magneto-crystalline anisotropy, and magnetoelastic anisotropy. Shape anisotropy is result from the geometric shape and the magnetization distribution of the materials. Certain shapes can promote the alignment of magnetic domains along specific axes, leading to different magnetic behaviors when the material is magnetized in various directions. For example, the demagnetizing field is minimized when the magnetization is aligned with the thin rod ferromagnetic material is shown in Figure1.1[1], so the magnetization exhibits unique responses when subjected to the field along its short or long axis, $H_{||}$ is the longest dimension of the material, and the energy of the system is lower in this configuration. The demagnetizing field can be expressed as $H_d = -NM$[1], where M is the magnetization, and N is the demagnetization factor that correlates to the shape of the material. For simple geometries like spheres, cylinders, and ellipsoids, the demagnetizing factors satisfy the condition: $N_x+N_y+N_z=1$[2]. For the ultrathin film case, the demagnetizing factors satisfy the condition: $N_x=N_y\cong 0, N_z\cong 1$. Therefore, the demagnetization field H_d direction is almost perpendicular to the plane. This means that there is a strong demagnetizing field acting against the magnetization that attempts to align perpendicular to the surface of the film. When we only consider the shape anisotropy in the thin film and neglect other effects,

doi:10.6342/NTU202403229

the film magnetization will naturally favor lying within the plane, which is referred to as an easy plane of magnetization. Conversely, the hard axis will be perpendicular to the plane.

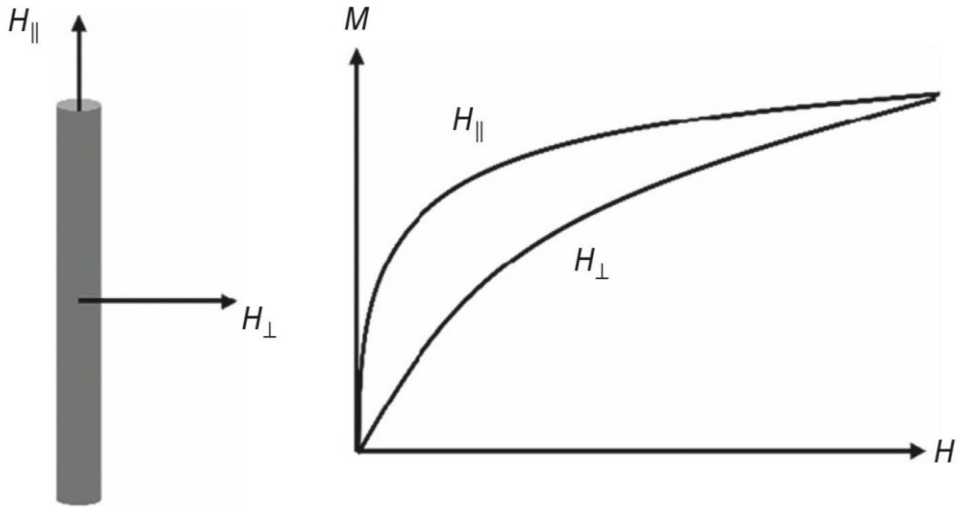

Figure 1.1 The easy (long) axis and the hard (short) axis of a ferromagnetic rod with elongated geometry. The magnetization will be harder to saturate along the short axis.[1]

1.1.2 Perpendicular magnetic anisotropy

For thin films, the demagnetization field is stronger along the direction perpendicular to the film's surface, typically resulting in an in-plane easy axis of magnetization. However, some magnetic materials can overcome this demagnetization effect and exhibit Perpendicular Magnetic Anisotropy (PMA). PMA refers to a type of magnetic anisotropy where the preferred direction of magnetization is perpendicular to the surface of the material. Transition metal-rare earth alloys, such as CoTb[3]、GdFeCo[4] and TbFeCo[5], are examples of materials that possess bulk PMA, where the strength of the PMA does not diminish as the thickness increases. However, some materials with heterostructure exhibit interfacial PMA, which originates from the interaction at the

doi:10.6342/NTU202403229

interface between the layers and strongly depends on the layers' thickness. For example, CoFeB/MgO interface has been widely demonstrated to present a strong interfacial PMA. This interfacial PMA arises from the hybridization of FeCo 3d and oxygen 2p orbitals at the CoFeB/MgO interface[6]. It is worth noting that the annealing process is necessary to achieve stable PMA in the CoFeB/MgO interface because the overall crystallinity will be improved through the boron diffuse out of the CoFeB layer [7]. Another typical system that presents PMA of interfacial origin is the Pt/Co system, which doesn't require an annealing process to induce PMA. The origin of the PMA in the Pt/Co interface is under debate, and several factors have been suggested that contribute to PMA. Some reports suggest that the PMA is probably related to the presence of chemically mixed Pt-Co interfaces[8]. Other reports attribute the origin of PMA to the direct Pt-Co hybridization at the interface[9]. Additional sources propose that magneto-crystalline anisotropy and strain-induced magnetoelastic anisotropy could also be possible origins[10].

1.2 Anisotropic Magnetoresistance

Anisotropic Magnetoresistance (AMR) refers to the phenomenon where magnetoresistance depends on the orientation of magnetization with respect to the direction of the current. AMR originates from the spin-orbit interaction within the material, which influences s-d electron scattering processes[11]. When a ferromagnetic material is magnetized, its resistance is not uniform in all directions. As shown in Fig 1.2[12], when the electric current I flows parallel to the magnetization M, the resistance is typically higher than when I flows perpendicular to M. This is because the 3d electron cloud is perpendicular to the current when I is parallel to M and is parallel to the current when I is perpendicular to M, leading to a larger cross-section for scattering when I is parallel to M. The angular dependence of the resistivity is given by[13] :

$$\rho(\theta) = \rho_{\perp} + (\rho_{\parallel} - \rho_{\perp}) \cos^2 \theta \tag{1.1}$$

doi:10.6342/NTU202403229

, and the magnitude of AMR can be quantified as[11] :

$$AMR = \frac{\rho(\theta)-\rho_{\perp}}{\rho_{\perp}} \quad (1.2)$$

, where θ is the angle between the current and magnetization direction, $\rho_{\perp}$ is the resistivity when the current is perpendicular to the magnetization direction, and $\rho_{\parallel}$ is the resistivity when the current is perpendicular to the magnetization direction.

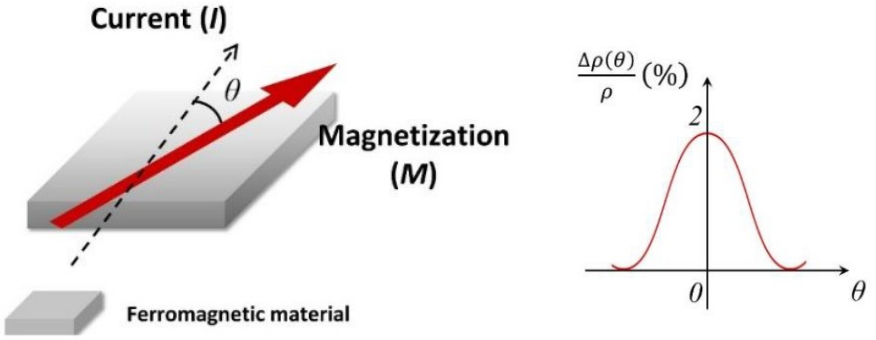

Figure 1.2 Diagram illustrating anisotropic magnetoresistance (AMR) effects[12].

doi:10.6342/NTU202403229

1.3 Magnetization dynamics

1.3.1 Landau-Lifshitz-Gilbert Equation

Landau-Lifshitz-Gilbert Equation(LLG equation) is a fundamental equation in the field of magnetism that describes the dynamic of the magnetization in the magnetic materials. It combines the principles of classical mechanics and quantum magnetic to provide insights into the behavior of magnetic systems. This equation primarily consists of two main components, which is the precession term and the damping term, and can be expressed as

$$\frac{dm}{dt} = -\gamma m \times H_{eff} + \alpha m \times \frac{dm}{dt} \tag{1.3}$$

, where γ is the gyromagnetic ratio, m is the magnetic moment vector, α is the damping constant, and H_{eff} is the effective magnetic field, which may include externally applied magnetic fields and the magnetic anisotropy field. The precession term arise from the interaction between the external field and the magnetization. As shown in Fig 1.3, when an external field is applied, the magnetic moment will rotates around the effective magnetic field. This is a non-dissipative process, meaning it does not involve energy loss. On the other hand, the damping term describe how the magnetic moment aligns with the effective magnetic field due to energy dissipation. By combining these two term, the LLG equation provides a description of how the magnetic moment gradually reaches a stable state through precession and damping when subjected to an external field.

doi:10.6342/NTU202403229

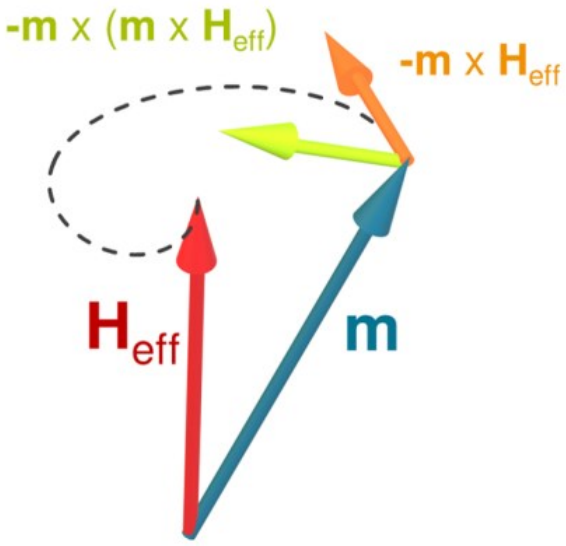

Figure 1.3 Magnetization dynamics time-dependent motion of the magnetization defined by Landau–Lifshitz–Gilbert (LLG) equation[14].

1.3.2 Spin-Orbit torque(SOT)

Spin-orbit torque (SOT) is a phenomenon where a spin current can exert a torque on the magnetization of materials. It arises from the spin-orbit interaction, which couples the spin and the angular momentum of the electrons. The typical SOT device is a ferromagnetic material that deposited on a heavy metal with strong spin-orbit coupling. When the electron flows through the heavy metal, there are spin accumulate at the edges of the bilayer interface. This spin current is then injected into the adjacent ferromagnetic layer and exerts a torque on the magnetization, which is known as the spin-orbit torque. The spin-orbit torque contains the damping-like torque τ_{DL} and the field-like torque τ_{FL}, and the motion of the moment in the ferromagnetic layer can be expressed as:

$$\frac{dm}{dt} = -\gamma m \times H_{eff} + \alpha m \times \frac{dm}{dt} + \tau_{DL}\left(\hat{m} \times (\hat{m} \times \hat{\sigma})\right) + \tau_{FL}(\hat{m} \times \hat{\sigma}) \qquad (1.4)$$

doi:10.6342/NTU202403229

The spin Hall angle θ_{SH} is a parameter to determine the efficiency of the SOT, and its' sign indicates the direction of the spin accumulation $\hat{\sigma}$ at the edge of samples. The signs of the θ_{SH} depends on the heavy metal. For example, Pt have positive θ_{SH}, while W and Ta have negative θ_{SH} [15]. Moreover, the opposite θ_{SH} will result in an opposite damping-like torque and field-like torque, as shown in Fig 1.4.

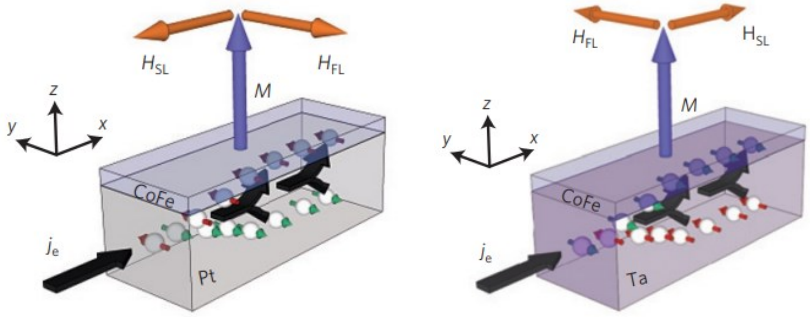

Figure 1.4 Illustration of the opposite direction of the SOT provided by Pt and Ta[16].

1.2.3 Ferromagnetic Resonance

Ferromagnetic Resonance (FMR) is an energy absorption phenomenon in ferromagnetic materials when exposed to a specific combination of static magnetic field and microwave field. When a ferromagnetic material is exposed to a static magnetic field and a microwave field, the microwave field excites the magnetic moments to precess around the direction of the effective magnetic field H_{eff}. As the frequency of an applied microwave field matches the intrinsic frequency of magnetic moment that precession in ferromagnetic material, the magnetic moments will resonate, leading to a significant absorption of energy from the microwave field, and the energy will finally lost by lattice vibration[17]. This intrinsic frequency is known as the ferromagnetic resonance frequency $\omega = \gamma \mu_0 H_{\text{eff}}$, and the absorption of energy can be characterized by a resonant absorption peak in the FMR spectrum, as shown in Fig 1.5. The effective field H_{eff} here

doi:10.6342/NTU202403229

contains the demagnetization field, microwave field, static field, and anisotropy field. The relationship between the resonance frequency and field can be expressed by the Kittel formula. If a sample experiences an in-plane magnetic field and only considers the shape anisotropy, the Kittel formula can be expressed in the following way[18]:

$$\omega = \gamma \sqrt{H - 4\pi(N_y - N_z)M_s}\sqrt{H - 4\pi(N_y - N_x)M_s} \tag{1.5}$$

,where N_x , N_y , and N_z are demagnetization factors, γ is the gyromagnetic ratio, and M_s is the saturation magnetization. If we consider the thin film sample which experience in the magnetic field that parallel to the in-plane direction. We can take $N_x = N_y \cong 0$, and $N_z \cong 1$.

Then, the equation can be simplified to the form:

$$\omega = \gamma \sqrt{H(H + 4\pi M_s)} \tag{1.6}$$

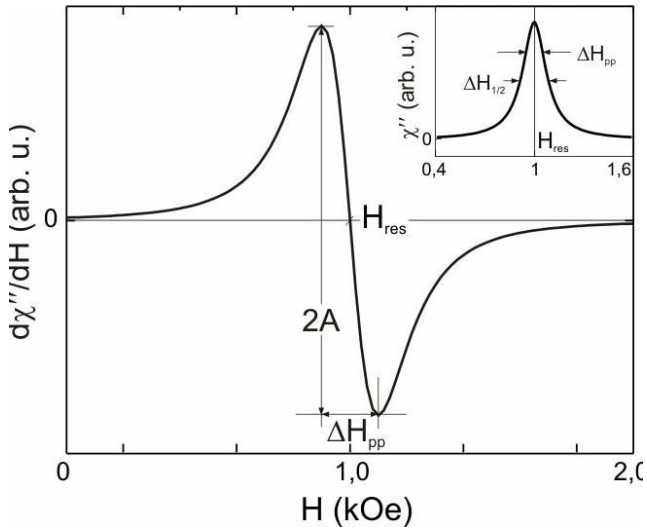

Figure 1.5 A typical FMR spectrum[19]

doi:10.6342/NTU202403229

1.4 Introduction of the inductor magnetic core

1.4.1 Magnetic core design consideration

The inductor is a fundamental passive component in an electrical circuit that stores energy from electrical energy in the magnetic field. The stored energy will used to regulate the current flow and, when combined with other electric components, can create various applications, such as voltage control, power harmonic filtering, and inverter current wave shaping in power supply applications [20, 21], as well as matching networks in wireless applications[22]. A magnetic inductor is composed of conductive wire and core material, and depending on the application, the core shape and material selection are investigated in various types[23]. With the development of modern technology, electronic devices are in demand for high speed and miniaturization, so high-performance inductor at high frequencies is increasingly required in industries. For an efficient inductor in the high-frequency application, ideal magnetic core materials are required to exhibit large permeability μ, high saturation magnetization M_s, high ferromagnetic resonance frequency f_r, high resistivity ρ, and low coercivity H_c [24]. The inductance of the inductor is proportional to the permeability, and magnetic materials often exhibit a larger permeability than non-magnetic materials. As a result, the inductor with a magnetic core can provide higher inductance than without a magnetic core. The permeability of the material can be expressed as $\mu = \frac{B}{H}$ [25], where B is the magnetic induction intensity, and H is the strength of the applied magnetic field. The permeability decreases when the H increases above the saturation field of the materials, so the high saturation magnetic materials are chosen to withstand the high current density. In addition, the permeability

doi:10.6342/NTU202403229

is also influenced by frequency. As the frequency increases, the energy loss occurs during the magnetization dynamics, and the permeability is expressed as a complex number[26] :

$$\mu(f) = \mu' + j\mu'' \tag{1.7}$$

, where the real part μ' is correspond to the energy store capacity of materials and the imaginary part μ'' is correspond to the energy loss of the materials. A frequency dependence of the permeability spectrum is shown in Fig 1.6. When the frequency nears the ferromagnetic resonance frequency f_γ of the materials, the imaginary part will increase significantly and reach maximum at the f_γ. At the same time, the real part permeability will drop significantly, which results in the inductance enhancement due to the magnetic material becoming negligible[27]. Therefore, materials with high ferromagnetic resonance frequency can provide a wider operating bandwidth for the inductor. However, it's challenging to obtain high resonance ferromagnetic frequency and high permeability simultaneously since there is often a trade-off relation between them, which is given by the Acher's limit[28]:

$$(\mu_i - 1)f_r^2 = (\frac{\gamma}{2\pi}4\pi M_s)^2 \tag{1.8}$$

, where the μ_i is the initial permeability that describes the permeability of a material at low values of magnetic induction intensity.

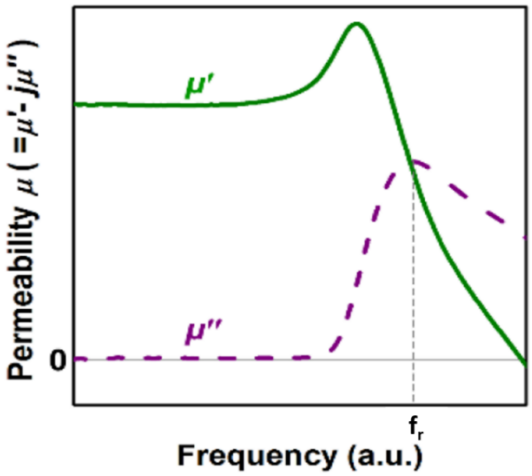

Figure 1.6 A typical frequency dependence of permeability spectrum[26].

doi:10.6342/NTU202403229

1.4.2 The core loss of the magnetic inductor

Inductor power loss is a crucial aspect in the design of inductors, particularly in high-frequency and high-power supply applications. The power loss of the inductor can be broken down into two components, which are the magnetic core loss and the winding loss. The core loss is generally categorized into two main components, which are the Eddy current loss and the Hysteresis loss [29, 30].

1.4.2.1 Eddy current loss

Eddy current loss occurs when a conductor is exposed to an alternating magnetic field. According to Faraday's Law, the change in magnetic flux will induce an electromotive force (EMF) in the conductor, giving rise to the circulate current in the conductor, and the induced circulate current is called Eddy current. This circulation current will dissipate in the form of heat, known as Eddy current loss. The Eddy current loss is inversely proportional to the resistivity of the conductor; for this reason, some literature divided the magnetic core into thin sheets and laminated the cores to reduce the path of the eddy current[31, 32]. Other literature fabricated magnetic materials coated with different insulating materials to increase the resistivity and result in low eddy current loss[33, 34].

1.4.2.2 Hysteresis loss

When a material is subjected to an applied field, the relationship between the material's flux density and the applied field strength can be represented by a hysteresis loop, as shown in Figure 1.7[35]. As the material experiences the magnetic field from

doi:10.6342/NTU202403229

zero to the saturated value and back to zero, the energy causes the domain wall to move and the domains to reorient, and finally, some energy is dissipated in the form of heat. This results in the returned energy being less than the supplied power, and the loss of the energy is called Hysteresis loss. Hysteresis loss is proportional to the area enclosed by the hysteresis loop[36], so it's generally proportional to coercivity in magnetic materials. Materials with higher coercivity tend to have wider hysteresis loops[37], which leads to greater energy loss during each magnetization cycle.

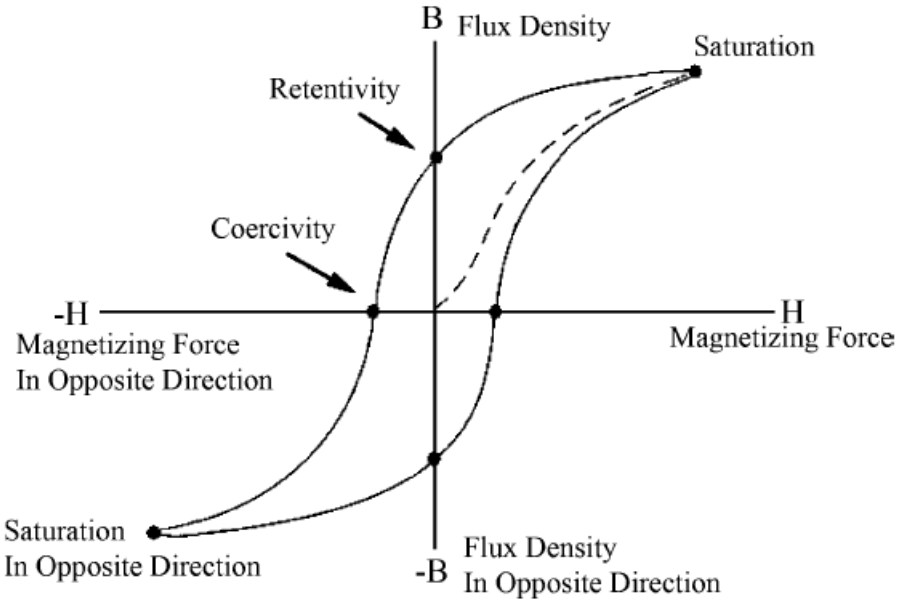

Figure 1.7 A hysteresis loop for a magnetic material[35].

doi:10.6342/NTU202403229

1.5 Motivation of this work

As mentioned in the previous section, the performance of a magnetic inductor at high frequencies is closely related to the magnetic core materials. Magnetic materials with high permeability provide significant improvements in inductance but are simultaneously limited by the ferromagnetic resonance frequency and core loss at high frequencies. When the frequency reaches the ferromagnetic resonance frequency, the material absorbs the energy from the alternating magnetic field, and the permeability drops to unity, resulting in poor performance of the inductor. The resonance frequency of magnetic thin film materials is typically in the range of 1-2 GHz[38]. However, many wireless communication applications operate at several GHz nowadays, such as mobile devices[38], Bluetooth[39], and the Global Positioning System (GPS)[40], indicating the integrated inductor with high operating frequency is indispensable. With the rapid growth of the wireless communication market, the operating frequency will be further increased. While the ferromagnetic resonance frequency defines the upper limit of the operating frequency in the magnetic-integrated inductor. Therefore, extending the ferromagnetic resonance frequency of the magnetic core materials to a higher bandwidth is crucial for integrated inductors in high-frequency applications. From the Kittel equation, the ferromagnetic resonance frequency f_r depends on the anisotropy field and the demagnetization of the materials[41]. Therefore, to enhance f_r, some works of literature control the demagnetization by patterning the magnetic core material into different shapes [42, 43]. Other researches are aimed at enhancing the in-plane uniaxial anisotropy of materials by using various deposition methods[44-50]or controlling the exchange coupling in multilayers[51, 52]. From the diagram of the resonance frequency versus the resonant field in present reports[53, 54], it can be observed that the magnetic thin film

doi:10.6342/NTU202403229

with Perpendicular magnetic anisotropy (PMA) enables high resonance frequency beyond 5GHz without an external bias magnetic field which is a significantly high value compared with the primarily in-plane uniaxial anisotropy materials in the literature. However, the use of PMA materials in inductor magnetic cores is less discussed.

To explore the promising candidates for inductor core materials in high-frequency applications, this thesis will investigate the ferromagnetic resonance and the coercivity in four PMA systems. I will tune the zero-field FMR frequency (f_0) of materials by modifying the interfacial PMA strength in these systems. Two systems of W/CoFeB/MgO and Pt/Co/Pt with different ferromagnetic layer thickness will be prepared first. After figuring out the optimal thickness of the ferromagnetic layer, another two systems of W/CoFeB/MgO multilayers and Pt/Co/Pt multilayers will be prepared with a fixed optimal ferromagnetic thickness. In addition, the coercivity (H_c) of each system will also be discussed. The zero-field FMR frequency and the anisotropy of the materials are investigated by the ST-FMR measurement, and the coercivity will be measured by AHE measurement.

doi:10.6342/NTU202403229

Chapter 2 Experiment method

2.1 Fabrication technique

2.1.1 Magnetron Sputtering

Magnetron sputtering is a physical vapor deposition (PVD) technique used to deposit thin films onto a substrate. As illustrated in Fig 2.1, a target material is placed in a vacuum chamber and a high voltage will be applied between the cathode and the anode. Meanwhile, the argon gas is introduced into the vacuum chamber. The voltage between the cathode and the anode will accelerate free electrons in the chamber, causing them to collide and ionize the argon atoms, creating positively charged argon ions. As shown in Fig 2.1(c), the combination of the positively charged argon ions and the free electrons forms a plasma and will be confined near the target surface by the magnetic field created by the magnetron. The positively charged argon ions in the plasma are accelerated towards the target, causing ions to collide with the target. Subsequently, the target atoms will be ejected through momentum transfer, which is illustrated in Fig 2.1(b). Finally, these sputtered target atoms will travel through the vacuum and deposit onto the substrate, forming a thin film.

In this thesis, the target material will be deposited for a few hundred seconds on the Si/SiO_2 substrates, and then the growth rates for the target material can then be estimated by the thickness measurement with the alpha-step. Thereafter, we can deposit the films with the desired thickness by controlling the sputtering time.

doi:10.6342/NTU202403229

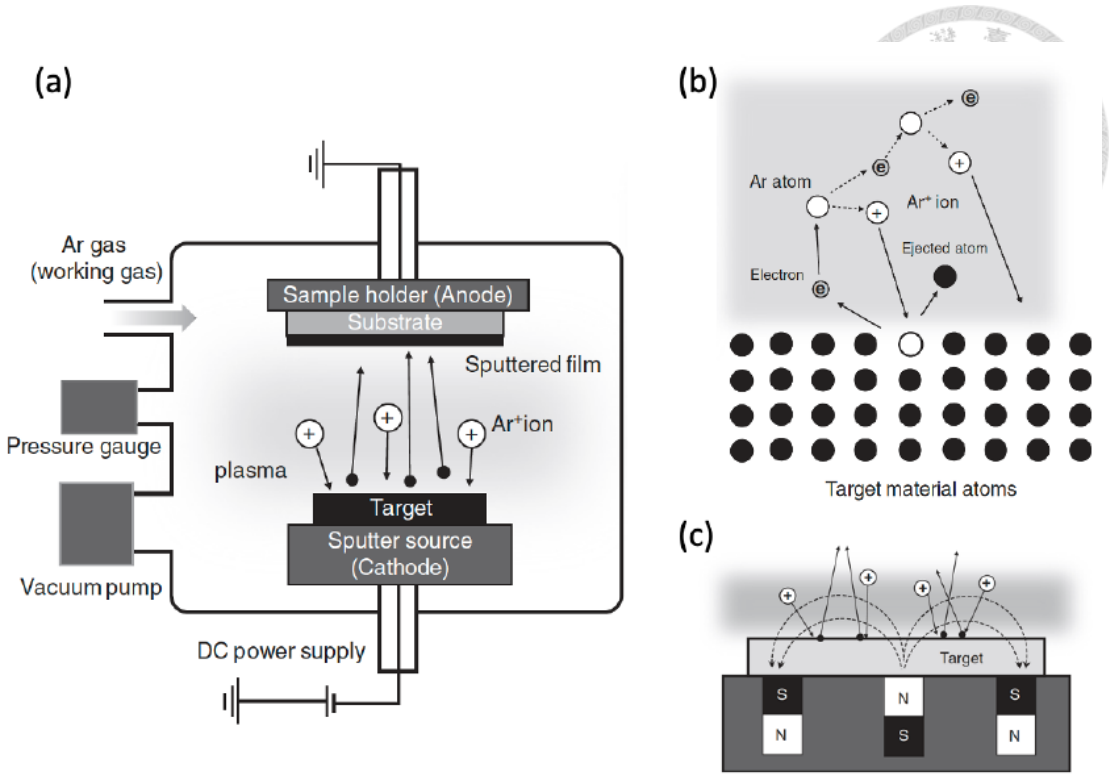

Figure 2.1 (a) Illustration of the magnetron sputtering system[1].(b)The process of the target atoms be ejected through the momentum transfer[1]. (c) The magnetic field created by the magnetron will confine the plasma to the area near the target surface[1].

2.1.2 Ion-beam etching

Ion-beam etching is a dry etching process that uses a beam of energetic ions to remove materials from the substrate, which is widely used in the fabrication of industry. As illustrated in Fig 2.2(a) , a substrate is on a rotating fixture with an adjustable tilt angle. A beam of ions is generated in an ion source. These high-energy ions will bombard the surface and collide with the surface atoms, causing atoms to be ejected from the surface. These ejected atoms will create a void where the photoresist doesn't protect the materials. This selective removal of materials will reproduce the mask pattern onto the substrate. To achieve a uniform etching result, the substrate is rotated during etching. The secondary ion mass spectrometry (SIMS) is commonly used as an endpoint detection method in ion

doi:10.6342/NTU202403229

beam etching to control the etching process precisely. When the ion bombard the surface during ion beam etching, a fraction of these ejected atoms will be ionized, forming secondary ions that contain information about the surface elemental composition, and then the SIMS detector will collect these secondary ions and analyzes them in a mass spectrometer. By monitoring the SIMS signal over time, the transitions between different layers in a multilayer structure can be detected, allowing the etching process to be stopped at the desired layer. Fig 2.2(b) shows a SIMS signal given by the Si/SiO_2/W/CoFeB/MgO/Ta sample during the etching process. Since the etching process is progressing from the top to bottom of the sample, the SIMS signal will rises in the opposite order to the layer stack order.

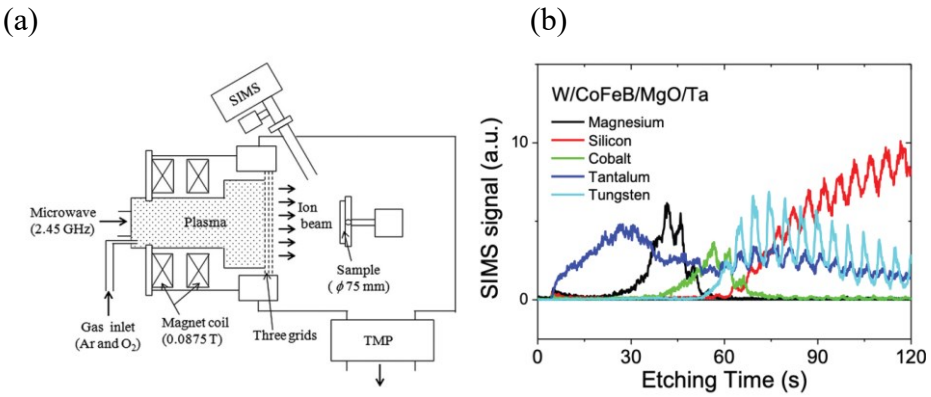

Figure 2.2 (a)Illustration of ion beam etching system[55].(b) The SIMS signal from the Si/SiO_2/W/CoFeB/MgO/Ta sample during etching process.

2.1.3 Sample preparation

In this thesis, the microstrip device and the Hall bar device will be prepared for the ST-FMR and the AHE measurement, respectively, as illustrated in Fig 2.4. The fabrication of the devices can be divided into two steps. In the first step, the film will be patterned into a stripe or Hall bar shape by the first mask and the etching process, as displayed in Fig 2.3(a). As for the second step, the pattern film from the first step will be capped with

doi:10.6342/NTU202403229

the electrode by the lift-off process and magnetron sputtering process, as displayed in Fig 2.3(b). The details of the photolithography process will be described below.

In the first step, the sputtered films will be baked at 100℃ for 60 seconds to remove the moisture. Afterward, the positive type photoresist is coated on the sputtered film by the spin-coating process, and the rotation rate of the spin-coater is 3000rpm for 10 seconds, then directly transitioning to 4000 rpm for 30 seconds. After coating the photoresist uniformly on the sputtered film, the film with the photoresist will be baked at 100℃ for 2 minutes to remove residual solvents from the spin-coated photoresist. Subsequently, the film will be exposed to the UV light through the mask with our desired pattern, where the exposure time for the UV light is 10 seconds. After the exposure process, the developer solution (TMAH) will selectively dissolve the exposed photoresist regions. The films of the dissolved photoresist region will be removed after the ion beam etching and then the film will be changed into the desired pattern. After the etching process, the acetone will be used to wash away the residual photoresist and the deposition materials on the top of the photoresist in the pattern. By following the similar photolithography process from the first step, the photoresist pattern for the electrode will be capped onto the first step pattern, and then the electrode will be deposited by magnetron sputtering. The structure for the electrode is Ta(80nm)/Pt(4nm).

doi:10.6342/NTU202403229

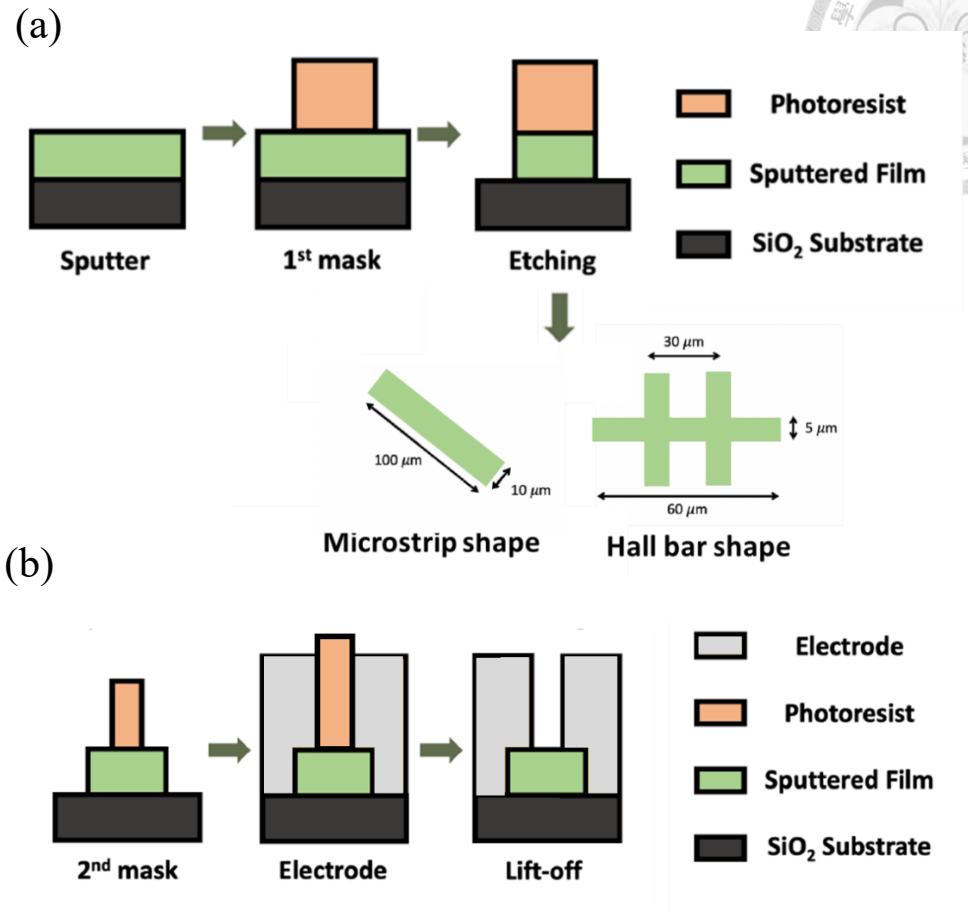

Figure 2.3 (a) Illustration of the first step process for photolithography (b) Illustration of the second step process for photolithography.

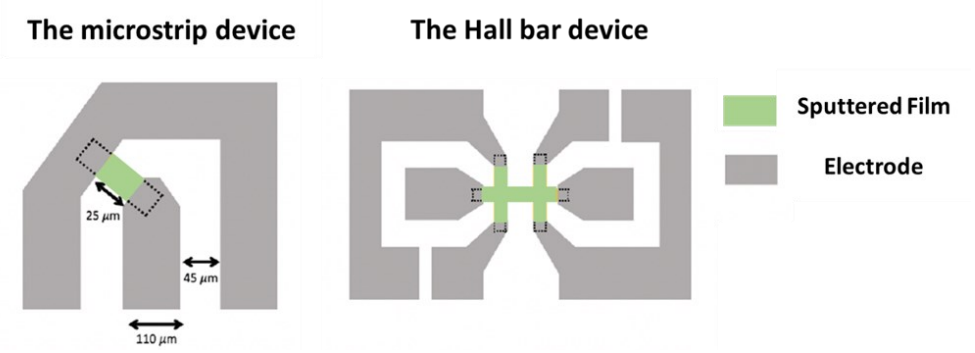

Figure 2.4 Illustration of the microstrip device and the Hall bar device.

doi:10.6342/NTU202403229

2.2 Measurement method

2.2.1 Anomalous Hall Effect (AHE) measurement

When an applied current passes through a conductor perpendicular to an external magnetic field, the electrons will deflect due to the Lorentz force. This deflection causes an additional electric field to be generated perpendicular to both the direction of the current and the magnetic field, resulting in a potential difference across the ends of the semiconductor or metal, and this phenomenon is known as the Ordinary Hall effect (OHE). While the Anomalous Hall Effect (AHE) is a phenomenon observed in certain magnetic materials, where it contributes an additional contribution in addition to the Ordinary Hall effect. When a current flows through a magnetic material, besides the Ordinary Hall effect caused by an external magnetic field, an additional voltage is generated. As shown in Fig 2.5[56], the Anomalous Hall Effect is mainly associated with three mechanisms, which are Intrinsic deflection, side jump, and skew scattering. The Intrinsic deflection arises from the Berry phase in the band structure, which gives electrons an additional velocity component that perpendicular to the electric field. While the side jump and skew scattering are originate from the spin-orbit interaction between electrons and impurities.

The AHE measurement is measured by the Hall bar device, and the measurement setup can be illustrated in Fig 2.6. The current I_x is applied by Keithley 2400 flows in the x-direction, and the Hall voltage V across the sample can be measured by the

doi:10.6342/NTU202403229

Keithley 2000. The Hall resistivity is the sum of the ordinary Hall component and the anomalous Hall component, which can be expressed as[57, 58]

$$\frac{Vd}{I_x} = \rho_{xy} = R_O\mu_0 H_z + R_A\mu_0 M_z \quad (2.1)$$

, where the d is the film thickness, ρ_{xy} is the total hall resistivity, H_z is the applied field along the z-direction, R_O is the ordinary hall coefficient, and the R_A is the anomalous hall coefficient. Because of the dominant signal from the anomalous hall component, we can obtain the information from the z-component of the magnetization M_z behavior from the measured signal.

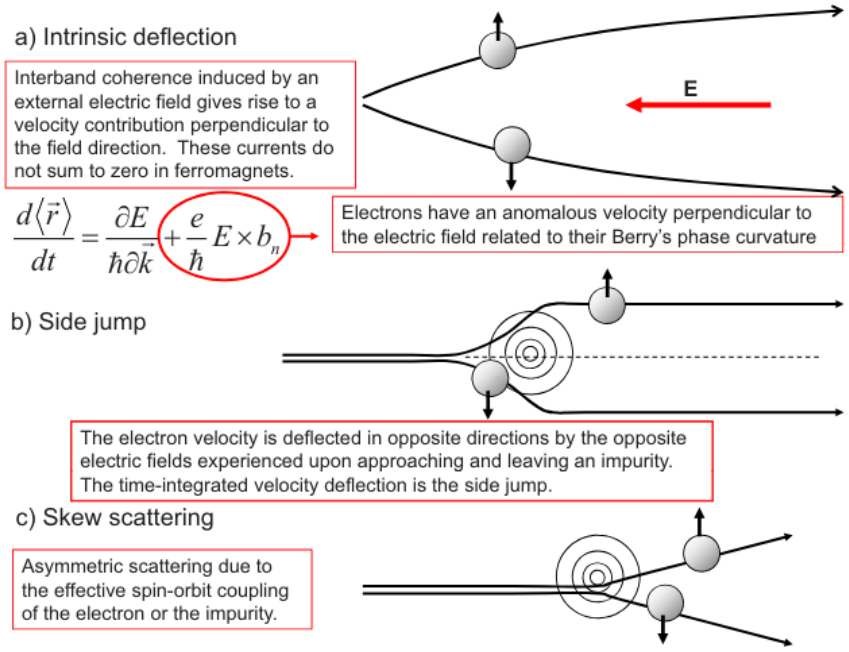

Figure 2.5 Illustration of the three mechanisms of AHE [56].

doi:10.6342/NTU202403229

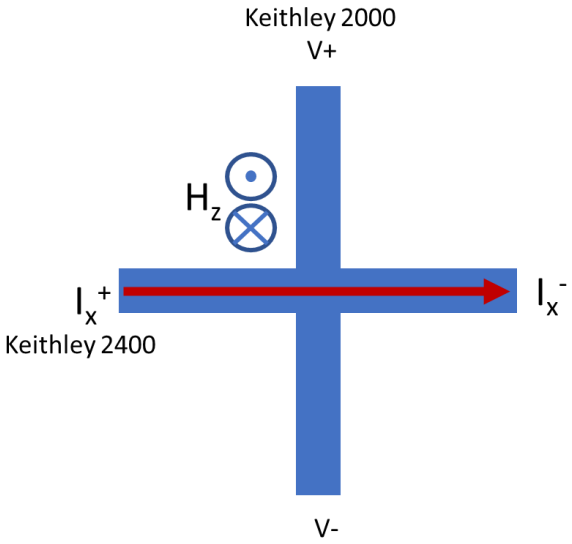

Figure 2.6 A sketch of the AHE measurement setup.

doi:10.6342/NTU202403229

2.2.2 Spin-Torque Ferromagnetic Resonance (ST-FMR) measurement

In the previous chapter, we have known that the alternating magnetic field will trigger the magnetization into precession, and the FMR occur when the frequency of an alternating magnetic field matches the intrinsic frequency of magnetization precession in the ferromagnetic material. However, besides the alternating magnetic field, the spin torque generated by an alternating current can also as a source to drive ferromagnetic resonance. This can be understood from the Fig 2.7(a) shown below. When a rf current (I_{RF}) is injected into a Pt layer, the spin-orbit interaction within Pt will produce an imbalance of spins accumulated at the Pt/Py interface due to the Spin Hall Effect (SHE)[59]. These imbalance spins will subsequently diffuse into the Py layer and exert a torque on the magnetization of the Py layer, namely the spin-orbit torque (SOT), which has been introduced in section 1,2,2. The rf Oersted field generated from the rf current will also exert a torque on the magnetization and together with the SOT to drive the magnetization into precession. The resulting precession phenomenon leads to oscillatory resistance due to the AMR effect. The oscillatory resistance $R(t)$ and the rf current $I(t)$ will produce a mixing voltage V_{mix}, which can be derived as below:

The oscillatory resistance will follow the form of AMR and can be expressed as

$$R(t) = R_{\perp} + (R_{\parallel} - R_{\perp})cos^2\theta(t) = R_{\perp} + \triangle R\, cos^2\theta(t) \tag{2.2}$$

, where θ is the angle between I and magnetization and can be expressed as

$$\theta(t) = \theta_H + \theta c \cdot \cos(\omega t + \delta) \tag{2.3}$$

, where θ_H, θc and δ are denoted the angle between I and the effective field, magnetization precession cone angle and the resonance phase between the driven force (SOT torque or the torque induced by Oersted field) and the magnetization response

doi:10.6342/NTU202403229

(oscillation of AMR) respectively. Due to θ_H is much larger than the θ_c, R(t) can be further simplified and expanded by the Taylor's expansion, then the resistance is

$$R(t) = R_{\perp} + \triangle R[cos^2(\theta_H) - sin(2\theta_H) \cdot \theta c \cdot cos\,(\omega t + \delta)] \quad (2.4)$$

The $V(t)$ can be calculated by taking the product of the rf current I(t) and oscillatory resistance $R(t)$ and can be expressed as

$$\begin{aligned} V(t) = I(t)R(t) &= Icos(\omega t)\{R_{\perp} + \triangle R[cos^2(\theta_H) - sin(2\theta_H) \cdot \theta c \cdot cos(\omega t + \delta)] \\ &= [IR_{\perp} + I \triangle Rcos^2(\theta_H)]cos(\omega t) - \frac{1}{2} I \triangle Rsin(2\theta_H) \cdot \theta c \cdot cos(2\omega t + \delta) \\ &- \frac{1}{2} I \triangle Rsin(2\theta_H) \cdot \theta c \cdot cos(\delta)] \end{aligned} \quad (2.5)$$

The first and second term of the $V(t)$ is the time-dependent term which is related to the frequency ω and 2ω. While the last term of the $V(t)$ is the time-independent term, which is the rectified STFMR signal V_{mix}, therefore,

$$V_{mix} = -\frac{1}{2} I \triangle R\sin(2\theta_H) \cdot \theta c \cdot \cos(\delta) \quad (2.6)$$

and can be measured from the voltmeter. In the STFMR measurement, when the rf current frequency (I_{RF}) and the external field (H_{ext}) meet the condition of the FMR, the δ from the out-of-plane torque (oersted field torque and field-like torque) will changes from 180° to 0° around the resonance field which is at 90°[60], so gives the antisymmetric Lorentzian line shape in the V_{mix} signal.(The blue line is indicated in the Fig 2.7(b)) While the δ from the in-plane torque (damping-like torque) will changes from 90° to -90° around the resonance field H_0 which is at 90°, so it gives the symmetric Lorentzian line shape in the V_{mix} signal. (The green line is indicated in Figure 2.7(b)). The sum of the antisymmetric and symmetric Lorentzian is the signal that we detect from the STFMR measurement, and the signal can be fitted by the fitting function[61],

$$V_{mix} = V_S \frac{\triangle^2}{\triangle^2 + (H_{ext} - H_0)^2} + V_A \frac{\triangle(H_{ext} - H_0)}{\triangle^2 + (H_{ext} - H_0)^2} \quad (2.7)$$

where V_S are V_A is the amplitudes of the symmetric and antisymmetric Lorentzian, $\triangle$ is the linewidth of the measured signal, and H_{ext} is the external field.

doi:10.6342/NTU202403229

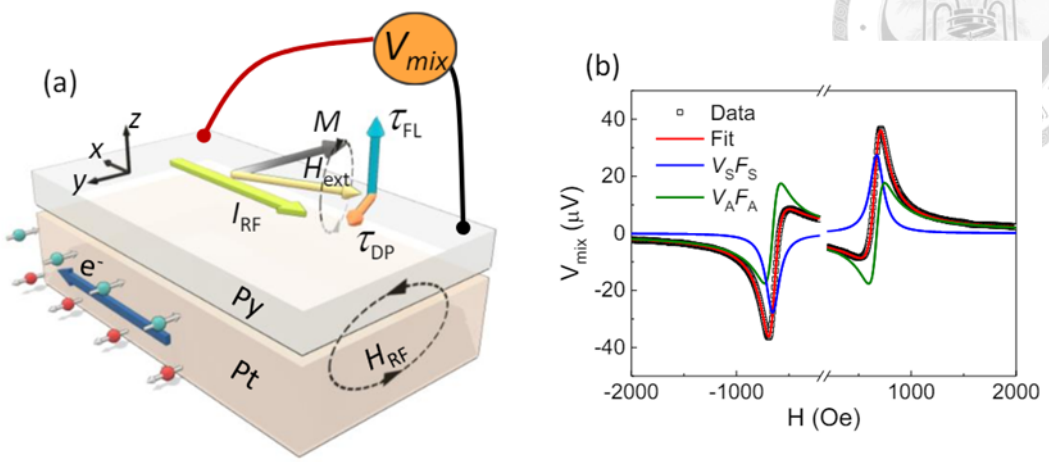

Figure 2.7 (a) Illustration of the STFMR measurement in Py/Pt heterostructure and (b) a typical ST-FMR signal spectra[62]

From the analysis of the signal, we can obtain the information about the magnetic properties and spin transport properties of the materials. The parameter V_s can provide the damping-like torque information, and V_s can provide the field-like torque and the Oreste field torque information. The resonance peak of the signal will shift when the rf current frequency changes, as shown in Fig 2.8[63], and this shift of the resonance peak will follow the Kittel equation. The Kittel equation may be derived as different expressions in different situations. As in the previous Chapter, we have discussed the Kittel equation in the case that only considers the demagnetization field. While in the materials with the other anisotropy, such as in-plane uniaxial anisotropy and the perpendicular anisotropy, the equation will express as [64, 65]

$$f_r = \frac{\gamma}{2\pi}[(H_0 + H_k)((H_0 + H_k + 4\pi M_{eff})]^{\frac{1}{2}} \quad (2.8)$$

, where the H_k is the in-plane uniaxial anisotropy field, H_0 is the resonance field, and the $4\pi M_{eff}$ is the effective demagnetization field, which consists of the shape anisotropy $4\pi M_s$ and the perpendicular anisotropy field $H_\perp$ and can be written into [65]

$$4\pi M_{eff} = 4\pi M_s - H_\perp \quad (2.9)$$

doi:10.6342/NTU202403229

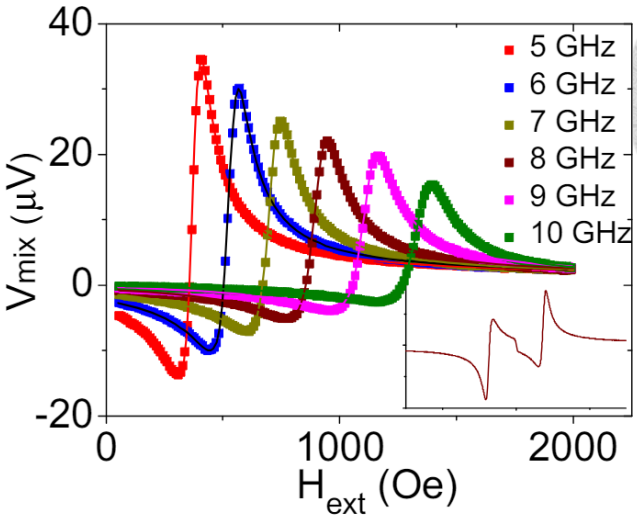

Figure 2.8 The resonance peak of the signal with the rf current frequency[63]

The STFMR setup in this thesis can be illustrated in Fig 2.9, the signal generator will provide rf current into the microstrip sample vias GS probe with the frequency range of 250kHz to 20GHz. Simultaneously, there is an external field applied at an in-plane angle of 45 degrees with respect to the rf current, then we can measure the signal by using the Lock-in amplifier and coupled with the bias-tee. The bias tee has three ports, which are connected to the signal generator, sample, and lock-in amplifier, respectively. The current from the signal generator passes through the bias tee and flows into the sample. The port connected to the lock-in amplifier will filter out the microwave current, allowing only the rectified STFMR signal to enter the lock-in amplifier, and the port connected to the signal generator will prevent the rectified STFMR signal from flowing into the signal generator.

doi:10.6342/NTU202403229

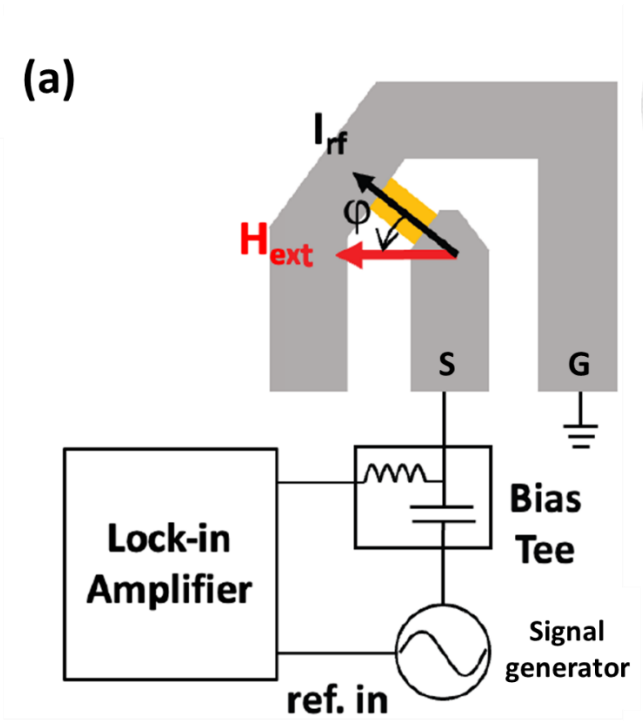

(b)

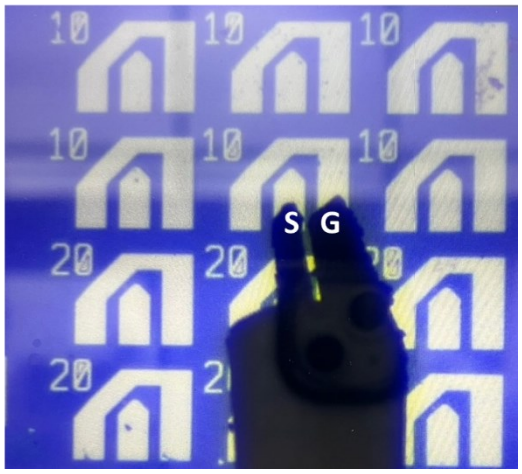

Figure 2.9(a) The illustration of the STFMR setup (b) The OM image of the GS probe on the $100\mu m \times 10\mu m$ microstrip sample.

doi:10.6342/NTU202403229

Chapter 3 Result and Discussion

In this thesis, the magnetic properties of interest for the core materials will be obtained from the ST-FMR and AHE measurements. The magnetic anisotropy and the ferromagnetic resonance frequency will be investigated by the ST-FMR measurement, while the coercivity field will be carried out by the AHE measurement.

3.1 Pt/Co/Pt system

As mentioned in section 1.1.2, the interface between the Pt and Co can produce interfacial PMA. Typically, the PMA present at the interface is strongly depend on the layer thickness, particularly when the ferromagnetic layer is thin. As the reason, a series of Ta(2)/Pt(2)/Co(t)/Pt(1)/Ta(2) with different Co thickness ranges from 1.2nm to 3.3 nm is studied in this section, where the units in parenthesis is in nanometers. The schematic diagram of the stack is displayed in Fig.3.1, where the bottom Ta layer of the stack is served as the buffer layer, and the upper Ta layer is the capping layer for preventing the specimen from oxidation. Both the two Pt layers adjacent to the Co can induce PMA in Co. In addition, the bottom Pt layer also serves as the spin current source. However, the upper Pt layer can also generate a spin current to the Co layer in a direction opposite to that of the bottom layer, and they may be canceled out with each other. Therefore, to avoid the absence of net spin current in the Co layer, the upper Pt layer is designed with a thinner thickness.

doi:10.6342/NTU202403229

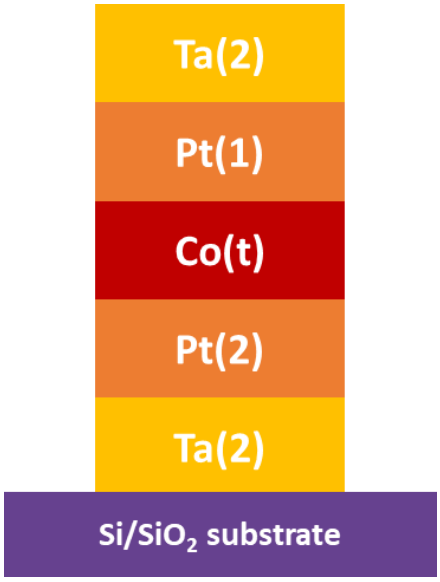

Figure 3.1The schematic diagram of the Ta(2)/Pt(2)/Co(t)/Pt(1)/Ta(2) stack

By applying a rf current at a fixed frequency and simultaneously sweeping the magnetic field during the ST-FMR measurement, we can generate the ST-FMR spectra depicted in Figure 3.2(a). Further analysis the resonance positions of the Lorentzian peaks in the frequency-dependent ST-FMR spectra, as illustrated in Figure 3.2(b), we can extract the effective demagnetization field $4\pi M_{eff}$ through the resonance frequency f_r as a function of resonance field H_0 by using the Kittel equation fitting, which is presented in Figure 3.2(c). The corresponding Kittel equation is expressed as follow:

$$f_r = \frac{\gamma}{2\pi}[H_0(H_0 + 4\pi M_{eff})]^{1/2} \quad (3.1)$$

Note that the $4\pi M_{eff}$ consists of the shape anisotropy $4\pi M_s$ and the perpendicular anisotropy field $H_\perp$ and can be expressed as $4\pi M_{eff} = 4\pi M_s - H_\perp$

doi:10.6342/NTU202403229

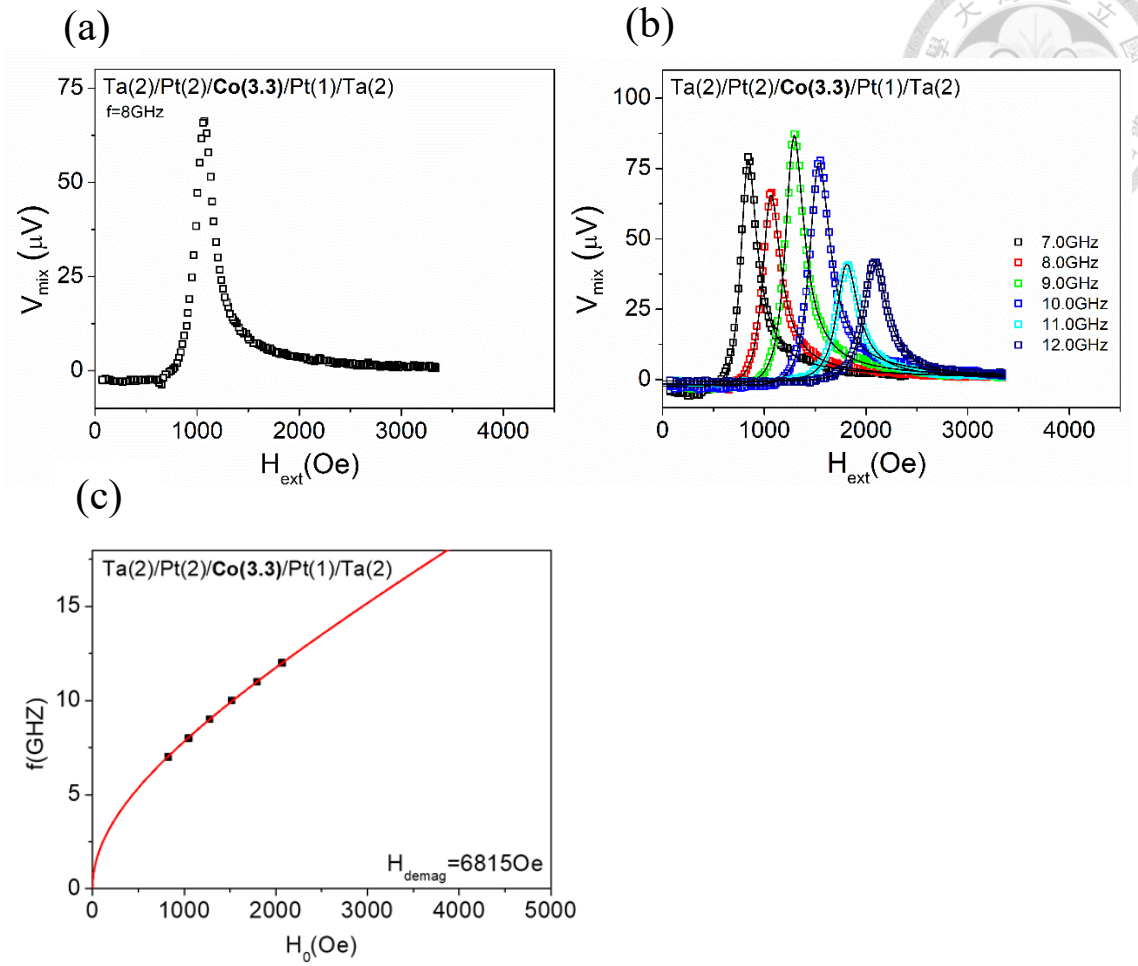

Figure 3.2 (a) The ST-FMR spectra of the Ta/Pt/Co(3.3)/Pt/Ta device at the rf frequency f=8GHz (b)Frequency-dependent ST-FMR spectra of the Ta/Pt/Co(3.3)/Pt/Ta device (c)The Kittel fitting of the Co Ta/Pt/Co(3.3)/Pt/Ta device.

Following the ST-FMR frequency-dependent measurement on all the Pt/Co/Pt series samples, the diagram of the frequency as a function of the resonance field for each sample can be summarized in Fig. 3.3, and the solid line is the fitting curves based on Kittel equation. From Fig. 3.3, it can be observed that the Kittel curves shift with the Co thickness. It is worth noting that the Kittel fitting curves in relatively thin Co layer samples present an addition branch in the low-field region, which indicates the existence of PMA[66]. The two branches mean that there are two resonance peaks can be observed in the STFMR spectra, as shown in Fig 3.4. However, it's difficult to observe two peaks

doi:10.6342/NTU202403229

simultaneously due to the limit of the measurement. The resonance peak in the low-field region for samples with Co thicknesses 1.4 nm and 1.5 nm is too indistinct for characterization, and the resonance peak in the high-field region from Co thickness 1.2 nm sample has reached the limit of the magnetic field that the instrument can provide.

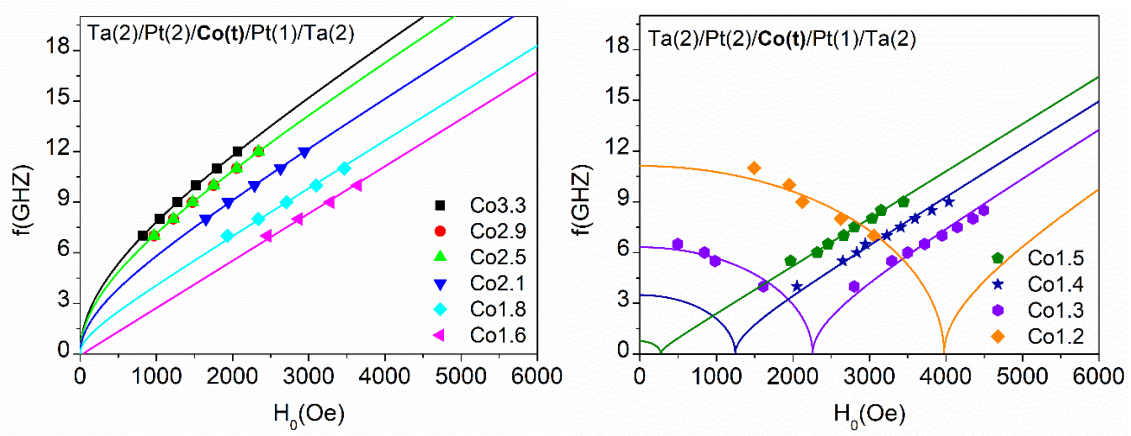

Figure 3.3 Frequency f as a function of resonance field H_0 for Pt/Co/Pt system samples with different Co thickness.

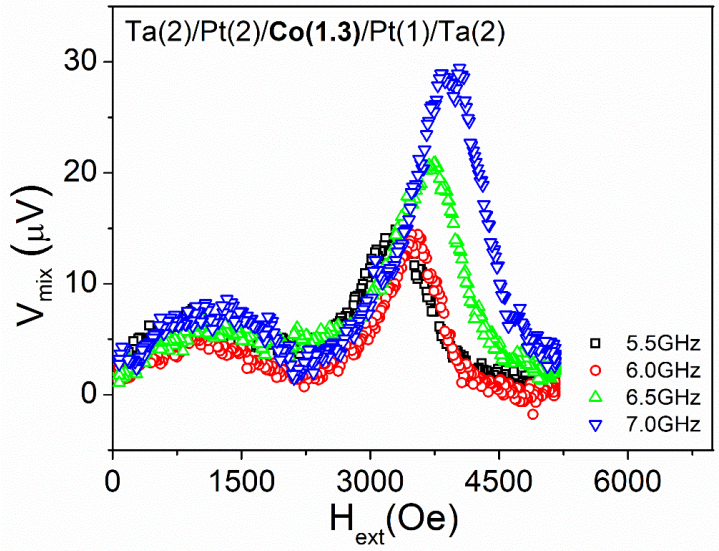

Figure 3.4 Two resonance peak ST-FMR spectra for Co thickness 1.3nm sample

The two peaks present in the PMA sample are fitted separately; the left branch from Fig 3.3 apparently doesn't follow the behavior described in equation 3.1 due to the external field is lower than the alignment field H_a^{FMR}, causing the magnetization will not

doi:10.6342/NTU202403229

be aligned with the external field[54]. While the behavior of the left branch can be derived as[53, 67]

$$f_r = \frac{\gamma}{2\pi}[\left(-4\pi M_{eff}\right)^2 - (H_0)^2]^{1/2} \quad (H_0 < H_a^{FMR}) \tag{3.2}$$

When the external field is larger than the alignment field, the magnetization will be aligned to in-plane from out-of-plane by the external field, and the signal behavior will be similar to the sample with in-plane anisotropy. Therefore, the right branch can still be fitted from the equation (3.1). Although we cannot simultaneously detect two resonance peaks in some PMA samples, the fitting equations for two branches are related to the parameter $4\pi M_{eff}$, allowing us to deduce the behavior of another branch by understanding one.

The extracted value of $4\pi M_{eff}$ as the Co thickness dependence is displayed in Fig.3.5 (a), the $4\pi M_{eff}$ shows a positive sign for relatively thick samples and a positive dependence on the Co thickness. When the Co thickness decreases to 1.6 nm, the $4\pi M_{eff}$ becomes negative. According to equation (3.2), this phenomenon indicates that the perpendicular anisotropy field increases as the thickness decreases, ultimately overcoming the demagnetization field at a Co thickness of 1.6 nm, causing the anisotropy of the system to change from in-plane to out-of-plane.

From Fig 3.3, we can observe that the resonance frequency at zero external field f_0 shifts away from 0 for the sample with perpendicular magnetic anisotropy. The dependence of f_0 on Co thickness is summarized in Fig 3.5(b), showing that f_0 increases as the perpendicular anisotropy increases. For the sample with a Co thickness of 1.2 nm, f_0 can be tuned up to 11.1 GHz due to the significant perpendicular magnetic anisotropy, which is consistent with our expectation.

doi:10.6342/NTU202403229

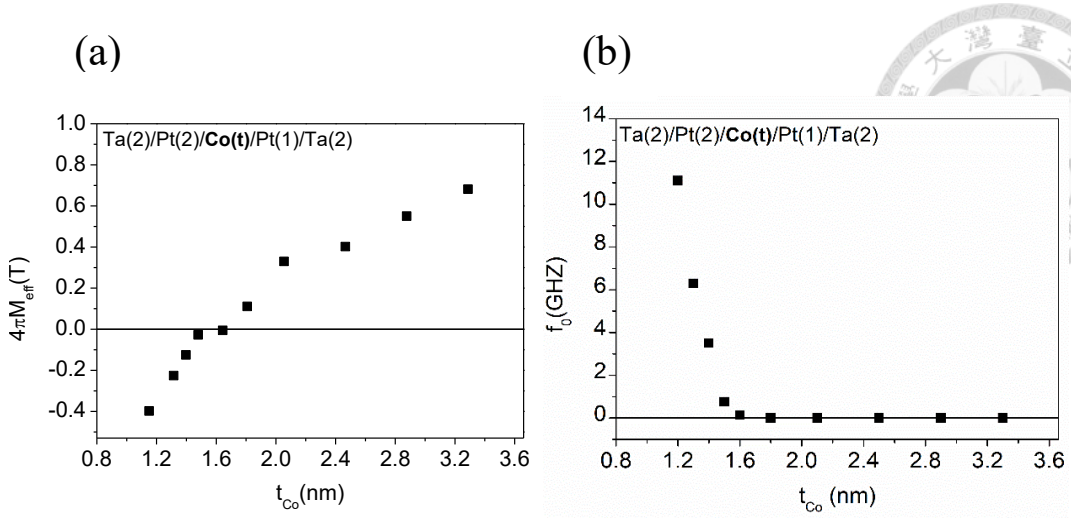

Figure 3.5 (a) The extracted value of $4\pi M_{eff}$ and (b) f_0 as Co thickness dependence.

To further enhance f_0, we have attempted to study samples with Co thickness less than 1.2 nm. However, for the PMA samples, the ST-FMR signal diminishes correspondingly as the Co thickness decreases and becomes undetectable at thicknesses less than 1.2 nm as illustrated in Fig. 3.6. This phenomenon is attributed to the small AMR effect with the thin Co thickness sample. According to equation (2.6), in order to obtain a strong ST-FMR signal, the AMR effect must be significant enough to produce a necessary resistance change, while the AMR effect decreases with the reduction of the Co film thickness due to the additional scattering from the interface or the current shunting in Pt layers[68, 69], leading to a reduction of the ST- FMR signal.

doi:10.6342/NTU202403229

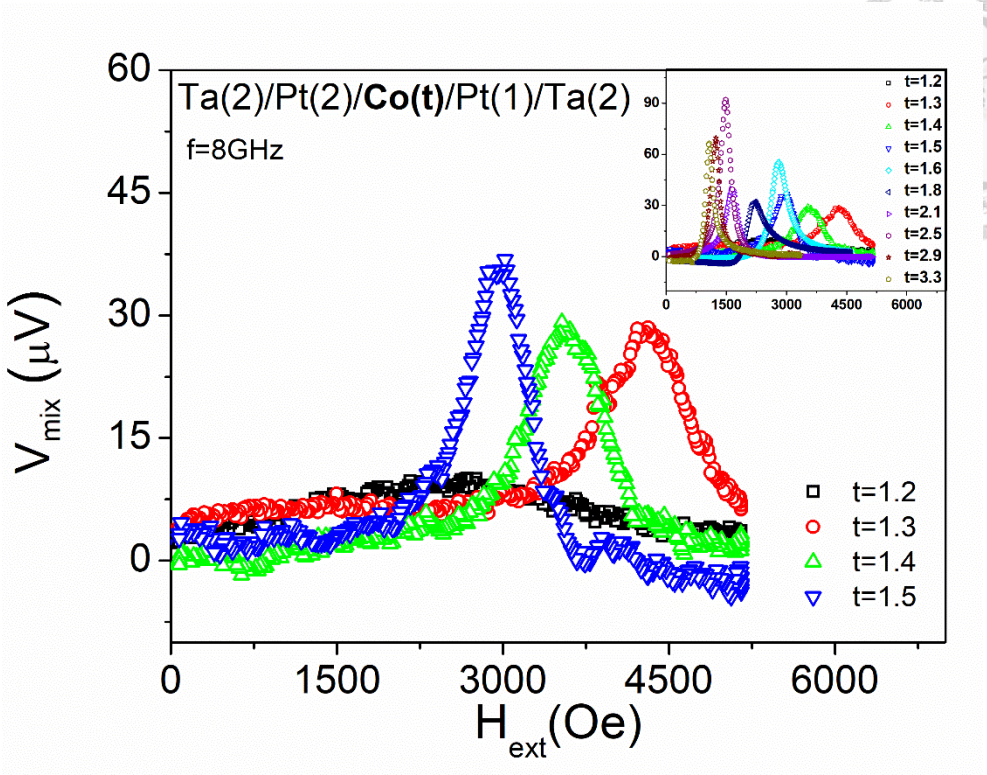

Figure 3.6 The STFMR spectra with different Co thickness at f=8GHz.

To consider the hysteresis loss for the design of the core materials, we measure the hysteresis loop in the PMA samples by the AHE measurement. As mentioned in section 1.4.2.2, the hysteresis loss of the core materials is proportional to the area enclosed by the hysteresis loop. The coercivity field H_c is the field required to reduce the magnetization to zero, therefore, material with higher coercivity exhibits a larger hysteresis loop area, so the H_c can be the parameter for describing hysteresis loss. The obtained value of the coercivity field H_c and the out-of-plane hysteresis loop for the PMA samples is displayed in Fig.3.7 (a) and (b), respectively. It can be observed that the H_c is shown to be inversely proportional to the Co film thickness and exhibits a considerable value of 130 Oe for the sample with a Co thickness of 1.2 nm, indicating a higher hysteresis loss compared with others.

doi:10.6342/NTU202403229

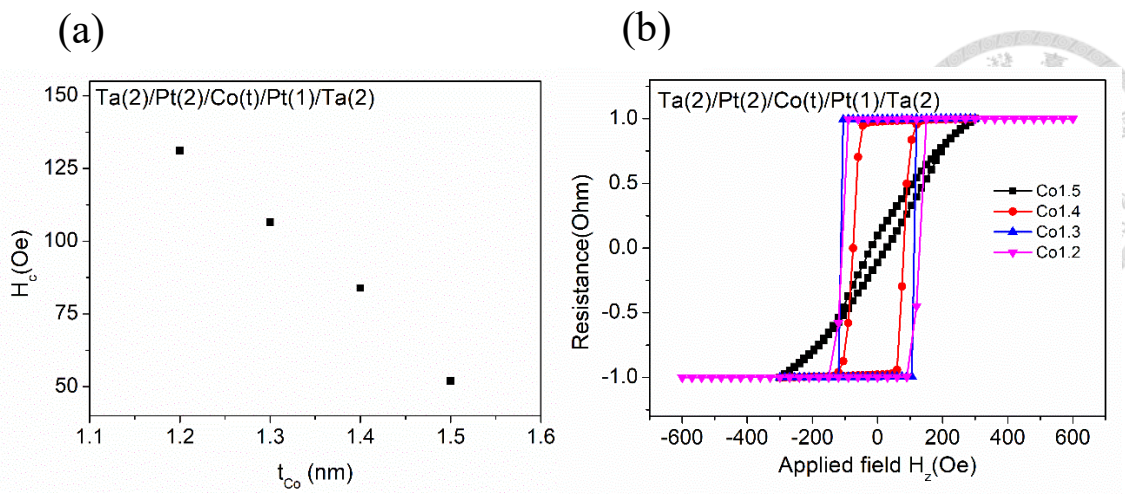

Figure 3.7 The obtained value of (a) coercivity field H_c and (b) the out-of-plane hysteresis loop for the PMA samples.

In summary, we successfully tuned the zero-field ferromagnetic resonance frequency f_0 by enhancing the PMA in the Pt/Co/Pt system. The PMA is enhanced as the Co thickness reduction, allowing f_0 to be correspondingly tuned up to 11.1 GHz when the Co thickness is reduced to 1.2 nm. However, the coercivity field H_c will also be increased as the Co thickness decreases in these PMA samples, and present a relatively high H_c of 130 Oe in the Co thickness 1.2 nm sample.

3.2 Pt/Co/Pt multilayer system

From the result of the previous section, a robust PMA with higher zero-field frequency is present only in the relatively thin Co layer in Pt/Co/Pt system. However, to substantially enhance the inductance, a comparable magnetic layer thickness is required for the core materials. Therefore, in this section, the Pt/Co/Pt multilayers will be prepared to increase the magnetic flux contribution from the Co layer. As shown in Fig 3.8, two structures of the Pt/Co/Pt multilayers will be prepared:

doi:10.6342/NTU202403229

The non-reversed structure Ta(2)/Pt(3)/[Pt(1)/Co(1)]$_n$/Pt(1)/Ta(2) and the reversed structure Ta(2)/Pt(1)/[Pt(1)/Co(1)]$_n$/Pt(3)/Ta(2), where n is the repetition numbers from 2 to 5 for the repeat layers, and Pt(3) serves as the spin source layer. The Co thickness of each layer is fixed at 1nm to induce large PMA at the Pt/Co interface.

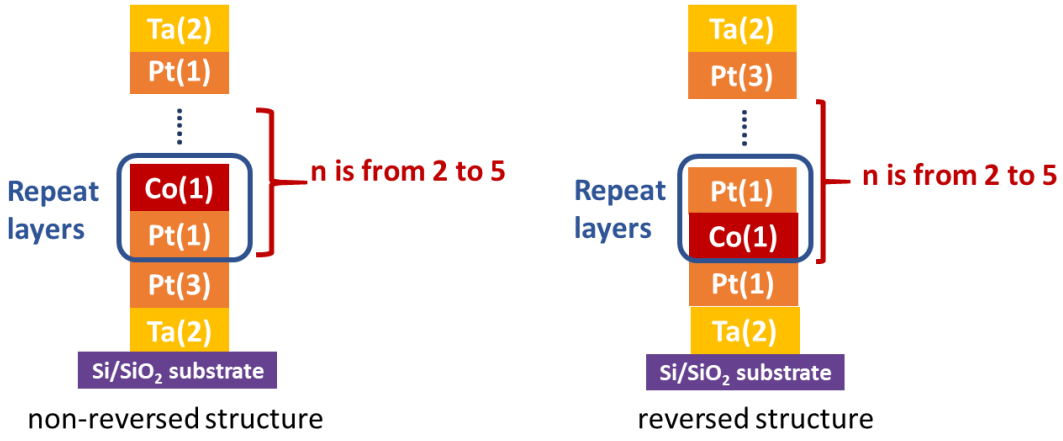

Figure 3.8 The illustration of the non-reversed structure and the reversed structure for the Pt/Co/Pt multilayers

The reason for n starts from 2 rather than 1 is because the ST-FMR signal from n=1 sample is undetected for both two structures. This is consistent with the results in the previous section, which state that the signal is absent when the Co thickness is less than 1.2 nm. However, the signal can be observed when n > 1, as displayed in Fig 3.9. This may be attributed to the overall AHE contribution from each Co layer increasing when n increases.

doi:10.6342/NTU202403229

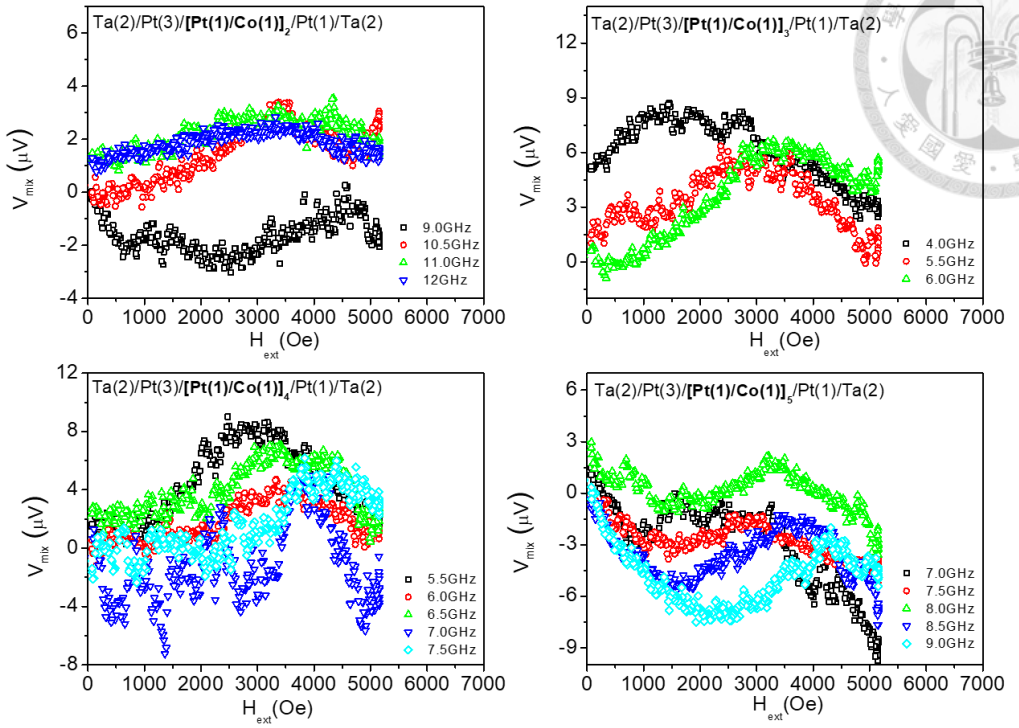

Figure 3.9 ST-FMR curves for the non-reversed structure samples.

Frequency as the function of resonance field and the $4\pi M_{eff}$ with different n for the non-reversed structure samples is displayed in Fig 3.10 (a) and (b), respectively. It can be observed that the $4\pi M_{eff}$ decreases as n increases, indicating the PMA deteriorates with n in the non-reversed structure. The extracted value of f_0 from Fig 3.10 (a) as n dependence is displayed in Fig 3.11. The f_0 decreases from 14.8 to 2.5 GHz as n increases from 2 to 5 because of the PMA deterioration. This PMA deterioration may be affected by the roughness. It has been reported that the PMA will deteriorate with large interface roughness in high repetition numbers[70]. During the deposition, local structural disorders such as atomic misfits and defects will accumulate, leading to a more significant roughness at high repetition numbers samples.

doi:10.6342/NTU202403229

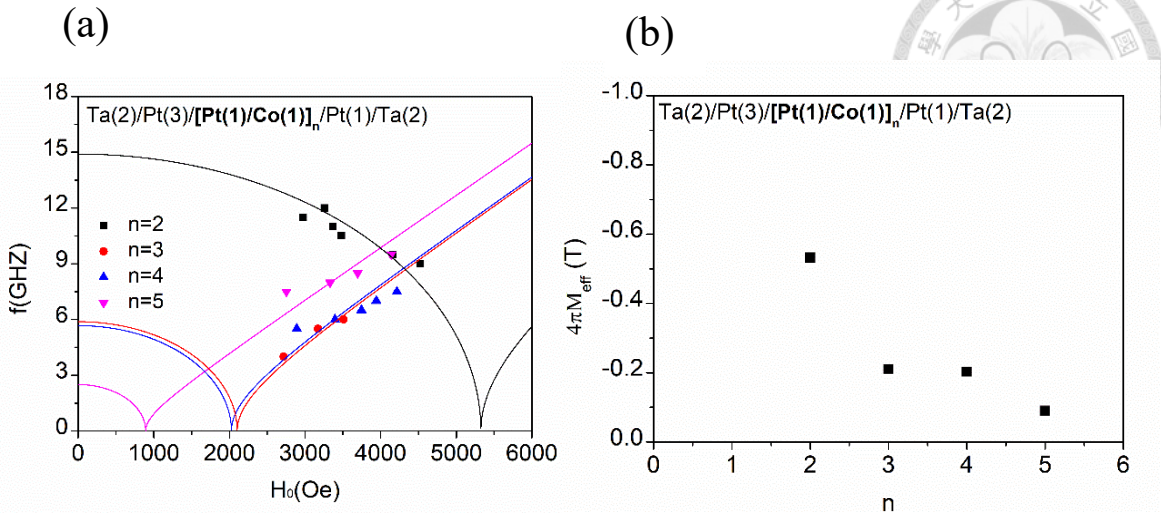

Figure 3.10 (a) Frequency f as the function of resonance field H_0 and (b) the $4\pi M_{eff}$ with different n for the non-reversed structure samples.

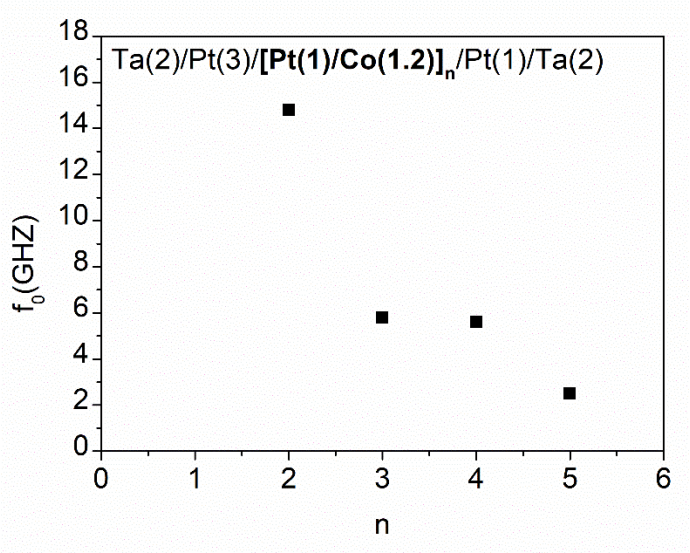

Figure 3.11 f_0 with different n for the non-reversed structure samples.

To minimize the impact of atomic misfits or defects on the PMA, the reversed structure is prepared. The repeats layer that provides PMA will be deposited before the spin source layer. The ST-FMR spectra from the reversed structure samples are displayed in Fig 3.12. Compared with the non-reversed structure, the transfer spin current that injects into the Co layers is in the opposite direction, so the detected signal from the reversed structure is reversed.

doi:10.6342/NTU202403229

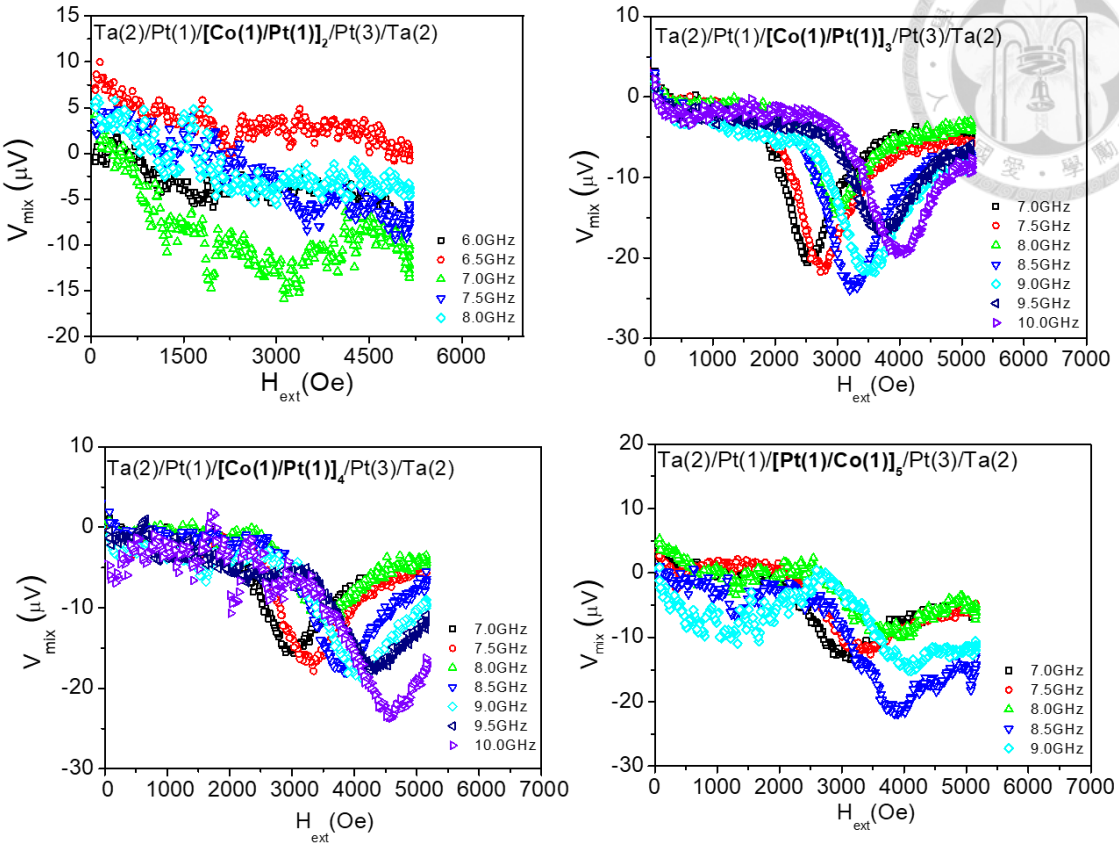

Figure 3.12 ST-FMR spectra with different n for the reversed structure.

Frequency as the function of resonance field for the reversed structure is displayed in Fig 3.13 (a), and the comparison of the $4\pi M_{eff}$ and f_0 with different n between two structures is displayed in Fig 3.13 (b) and (c). Compared with the non-reversed structure samples, the PMA strength in the reversed structure is weaker when n is from 2 to 3, but surpasses the non-reversed structure when n is 5. It has been found that the PMA strength in the Pt/Co/Pt multilayers increases when the thickness of the top Pt layers decreases because of the intermixing at the Co/Pt interface [71, 72]. Because Pt is significantly heavier and more strongly bonded than Co, more intermixing will occur at Co/Pt interface than at the Pt/Co interface. In contrast to the non-reversed structure, the top layer is thicker in the reversed structure, which may cause more atomic intermixing in the upper layers, resulting in weaker PMA strength. However, there is a striking trend of the PMA with n

doi:10.6342/NTU202403229

in the reversed structure samples. The PMA strength increases when n is from 3 to 5, which is opposite to the trend in the non-reversed structure. This implies that there is less roughness in the reversed structure, allowing it to maintain a more stable PMA compared to the non-reversed structure. However, this theory should be studied with more evidence. Some studies ascribe the rising of the PMA with n to the increases of the Pt/Co interface [73, 74], which promotes the magneto-elastic interface anisotropy induced by strain. This could potentially explain the trend of the PMA with n from 3 to 5 in the reversed structure samples.

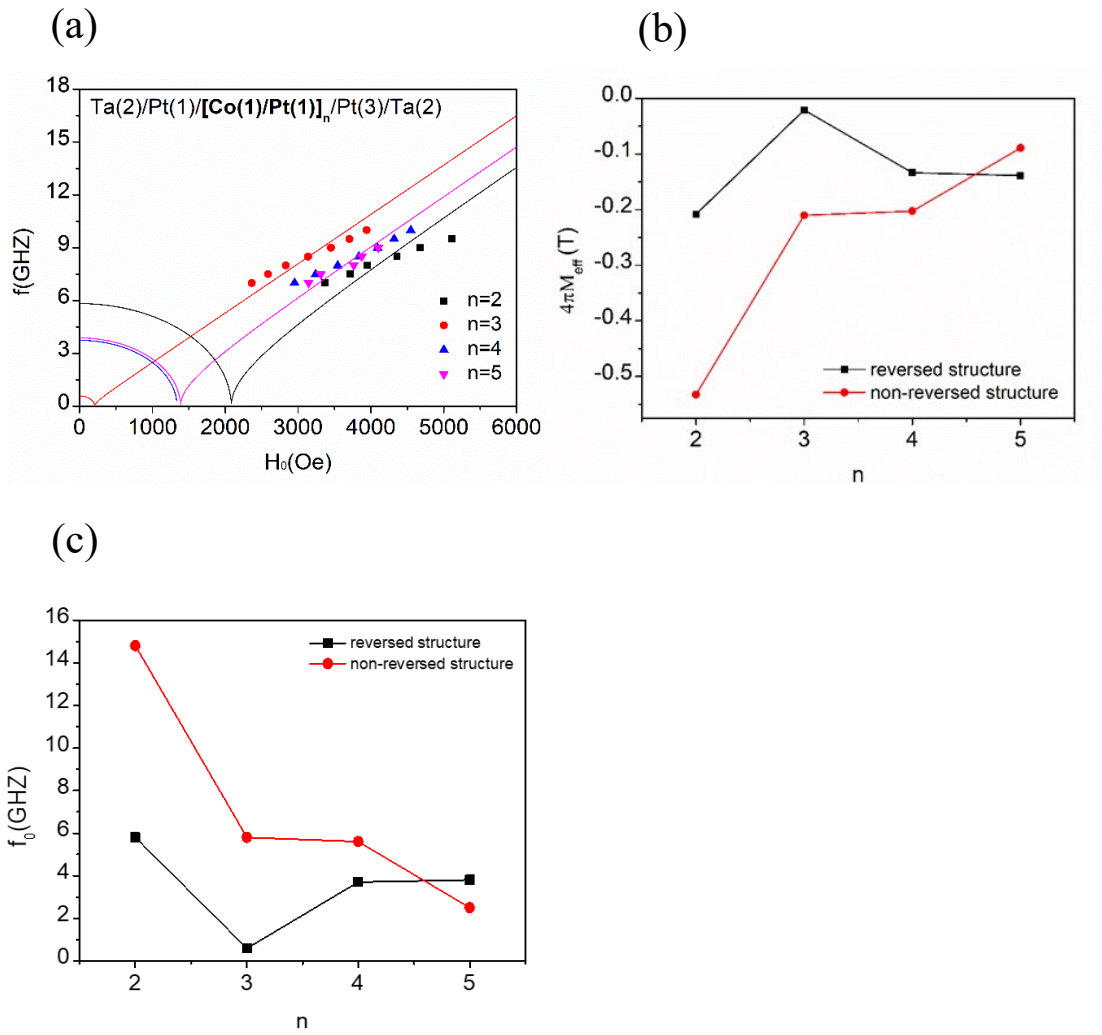

Figure 3.13 (a) Frequency f as the function of resonance field H_0, (b) the $4\pi M_{eff}$ and (c) f_0 with different n for the reversed structure samples and the non-reversed samples.

doi:10.6342/NTU202403229

The out-of-plane hysteresis loop for the non-reversed structure samples and the reversed structure are displayed in Fig 3.14 (a) and 3.14 (b), respectively. The comparison of H_c with different n between two structures is displayed in Fig 3.14(c). For the samples with the non-reversed structure, H_c is approximately 5 to 6 times larger than the reversed structure samples. When n increases to 5, H_c for the non-reversed and reversed structures is 302 Oe and 63 Oe, respectively. Some reports have found that the H_c is strongly dependence on the roughness, and it can be reduced when the surface roughness decreases[75, 76]. Compared to the samples with the non-reversed structure, the H_c of the samples with the reversed structure is much lower. This result suggests that the roughness may be smaller in the reversed structure than in the non-reversed structure, resulting in a more stable PMA in the reversed structure.

doi:10.6342/NTU202403229

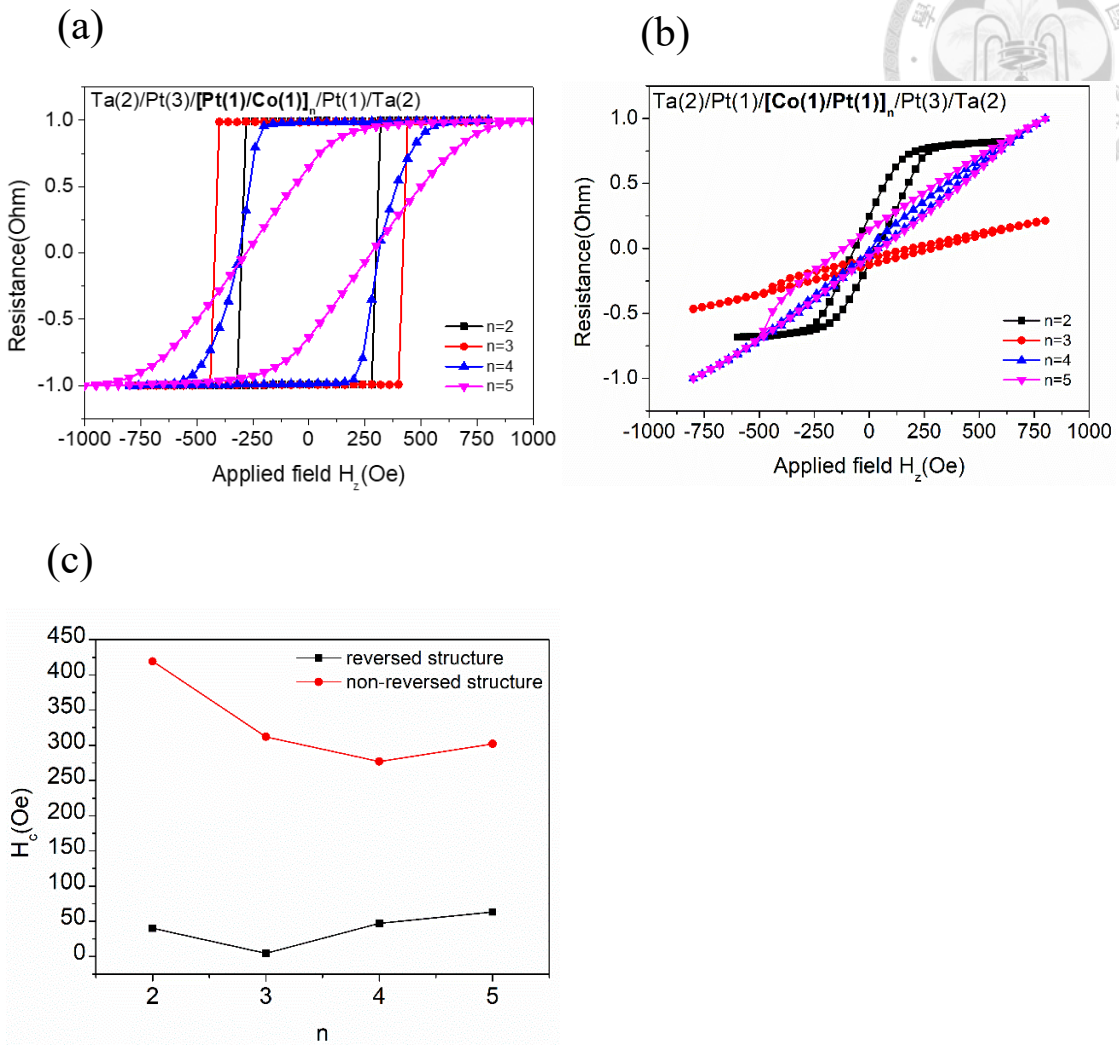

Figure 3.14 (a) The out-of-plane hysteresis loop for the non-reversed structure samples and (b) the reversed structure samples. (c) The H_c with different n for the reversed structure samples and the non-reversed samples.

In summary, two structures for the Pt/Co/Pt multilayers are prepared in this section. In contrast to the non-reversed structure, the reversed structure seems to maintain a more stable PMA in high repetition number samples, causing a higher f_0 of 3.8 GHz as n = 5. In addition, for the non-reversed structure samples, H_c is approximately 5 to 6 times larger than samples with reversed structure. When n increases to 5, H_c for the non-reversed and reversed structures is 302 Oe and 63 Oe, respectively.

doi:10.6342/NTU202403229

3.3 W/CoFeB/MgO system

In this section, another PMA system with the structure of W/CoFeB/MgO will be investigated. To achieve a strong PMA presence at the CoFeB/MgO interface, an annealing process is necessary to improve the structure crystallinity. Therefore, the annealed samples in W(4)/CoFeB(t=2, 2.5, 3)/MgO(2.3)/Ta(2) and W(4)/CoFeB(t=1.8, 2, 2.5)/MgO(2.3)/Ta(3) will be prepared, where the annealed temperature is at 300℃ for 1 hr. A series of the as-grown samples with W(4)/CoFeB(t=2, 2.5, 3)/MgO(2.3)/Ta(2) will be prepared as the control samples. The sketch for the samples structure in this section is shown in Fig 3.15. The W layer and the Ta layer for these samples are served as spin source layer and capping layer, respectively.

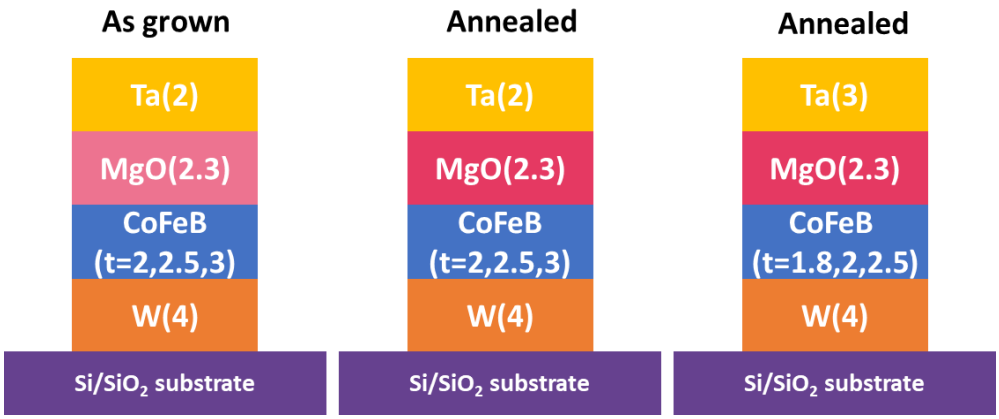

Figure 3.15 The schematic diagram of the sample structure in W/CoFeB/MgO system.

The ST-FMR spectra from all the CoFeB thickness 2.5nm samples can be illustrated in Fig 3.16. Because of the opposite spin hall angles between W and Pt, it can be observed that the signal is reversed in these W-based samples compared with the Pt-based sample in section 3.1. Although the signal from annealed W(4)/CoFeB(2.5)/MgO(2.3)/Ta(2) samples don't show a significant PMA feature, the ST-FMR curves shift toward the higher field after annealing, indicating that the PMA field is enhanced after annealing, according

doi:10.6342/NTU202403229

to equation (3.1) As shown in Fig 3.16 (c), when the capping layer is 3nm, a significantly PMA signature with two distinct curves can be observed, implying the PMA strength can be further enhanced when the capping layer increased from 2 to 3. These results may be attributed to the less oxidation of the thicker capping layer samples. However, it has been found that the MgO oxygen will diffuse into Ta and deteriorate PMA when the Ta capping layer thickness increases[77]. Therefore, besides CoFeB thickness, the Ta capping layer with an optimized thickness is also critical to attain high PMA. It's noted that the ST-FMR signal is undetected when the CoFeB layer is less than 2 nm for the capping layer thickness 2nm samples. However, when the capping layer thickness is 3nm, the thickness limit of the measurable signal can be further extended to 1.8nm, which may also related to the less oxidation in the sample.

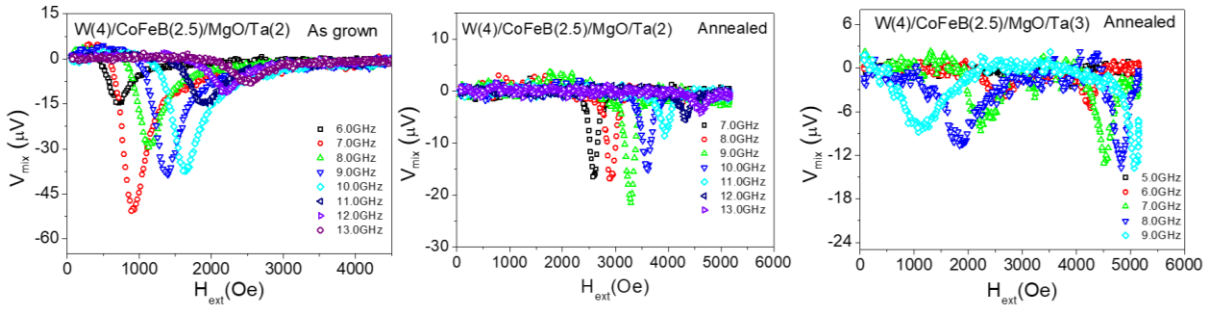

Figure 3.16 The ST-FMR spectra for (a) as grown W(4)/CoFeB(2.5)/MgO(2.3)/Ta(2) sample (b) annealed W(4)/CoFeB(2.5)/MgO(2.3)/Ta(2) sample, and (c) annealed W(4)/ CoFeB(2.5)/MgO(2.3)/Ta(3) sample.

Frequency as the function of the resonance field for all the as-grown samples and annealed samples is shown in Fig 3.17(a) and (b), respectively. It can be observed that the resonance frequency for all the as-grown samples shows in-plane anisotropy behavior with respect to the resonance field and follows well with the equation (3.1). As for the annealed samples, two branches can be observed in the samples with a relatively thin CoFeB layer, which is a signature of the PMA.

doi:10.6342/NTU202403229

The extracted value of $4\pi M_{eff}$ and f_0 of each sample by using equation (3.1) and equation (3.2) is summarized in Fig 3.17 (c) and (d), respectively. It can be observed that the $4\pi M_{eff}$ decreases with the CoFeB thickness decreases for all the annealed samples. When CoFeB thickness decreases to 2.5nm for the annealed samples with capping layer thickness 2nm, the signs of $4\pi M_{eff}$ changes to negative. This indicates that the anisotropy of the magnetization of the annealed samples with capping layer thickness of 2nm changes in-plane to out-of-plane at CoFeB thickness of 2.5nm. Comparing the same thickness annealed samples in W(4)/CoFeB(t)/MgO(2.3)/Ta(2) and W(4)/CoFeB(t)/MgO(2.3)/Ta(3) series, it shows a more negative value of $4\pi M_{eff}$ in W(4)/CoFeB(t)/MgO(2.3)/Ta(3) series, indicating the PMA can be further enhanced when the capping layer changes from 2 nm to 3 nm, and this result is consistent with the analysis from Fig. 3.16. There is also a significant enhancement of f_0 in the annealed samples when the capping layer changes. For the CoFeB thickness of 2.5 nm and 2 nm samples, f_0 increases approximately 10 GHz when capping layers change from 2nm to 3nm and reaches a maximum value of 21.6 GHz in the sample with a 1.8nm CoFeB.

doi:10.6342/NTU202403229

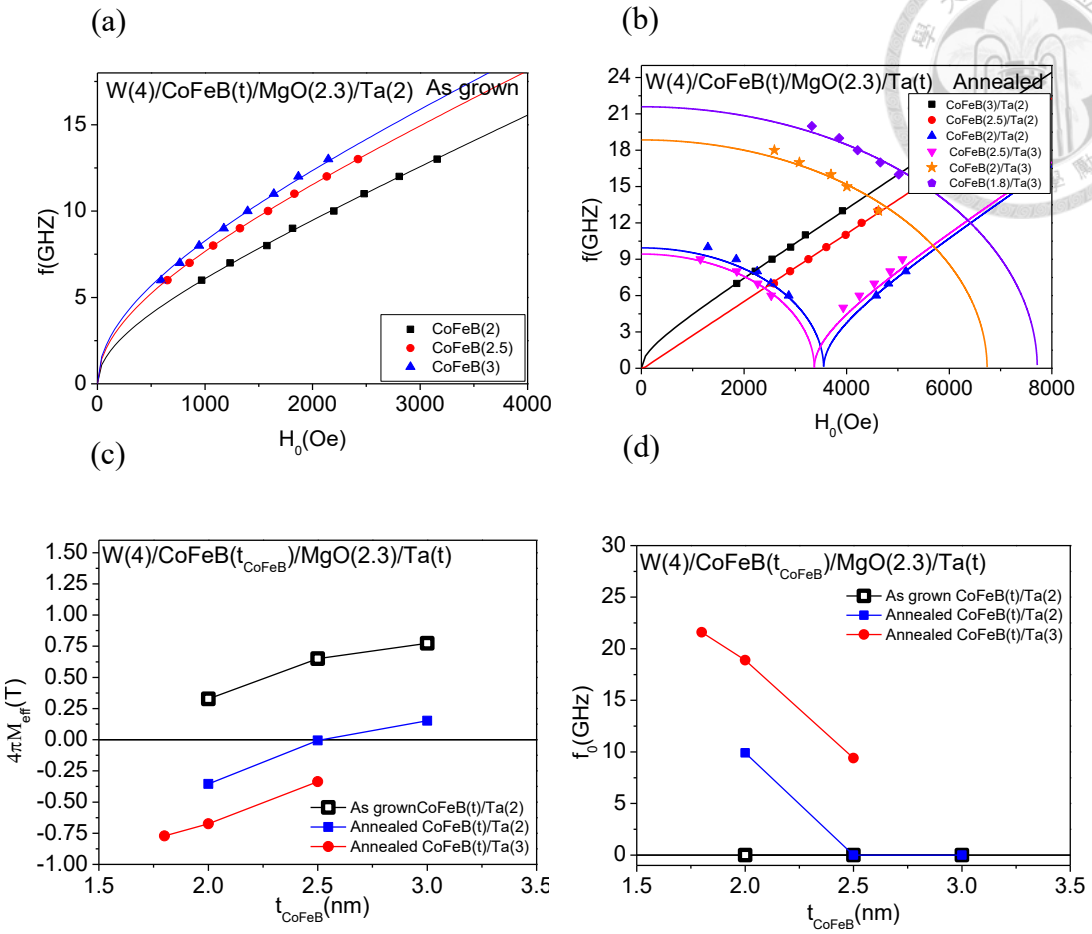

Figure 3.17 Frequency f as the function of the resonance field H_0 for (a) the as-grown samples and (b) the annealed samples. Summary of (c) $4\pi M_{eff}$ and (d) f_0 as CoFeB thickness dependence for all samples.

The out-of-plane hysteresis loop and H_c as CoFeB thickness dependence for the annealed samples with PMA is displayed in Fig 3.18 (a) and (b), respectively. The PMA samples in W(4)/CoFeB(t)/MgO(2.3)/Ta(3) exhibit higher H_c than the samples in the W(4)/CoFeB(t)/MgO(2.3)/Ta(2). For W(4)/CoFeB(t)/MgO(2.3)/Ta(3) with CoFeB thickness of 2.5 and 2 nm, H_c is at a constant around 37Oe, and it increases at 47Oe when CoFeB decreases to 1.8nm.

doi:10.6342/NTU202403229

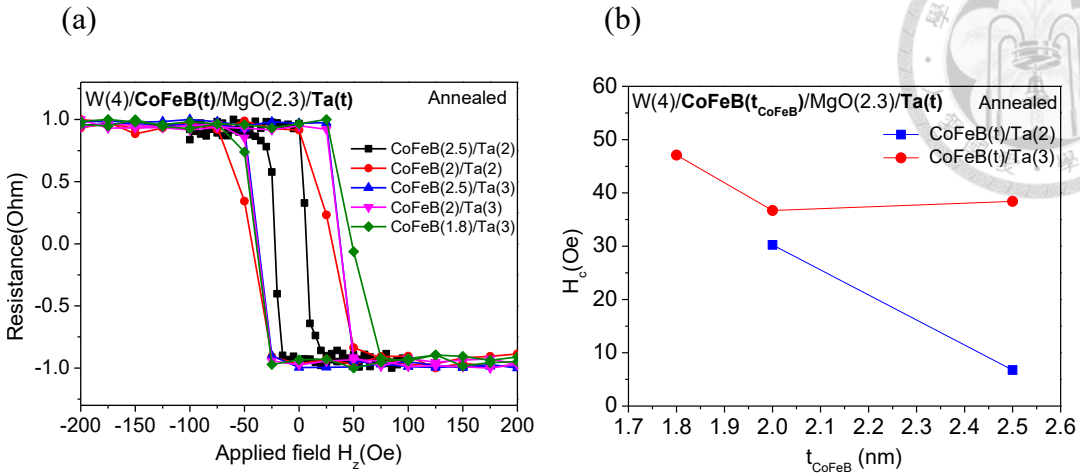

Figure 3.18 (a) The out-of-plane hysteresis loop for the annealed samples with PMA. H_c as CoFeB thickness dependence for the annealed samples with PMA.

In summary, the PMA presence in the annealed samples with CoFeB thickness less than 2.5nm and the strength of PMA is enhanced with CoFeB thickness reduction. Moreover, when the capping layer of the annealed samples changes from 2nm to 3nm, the PMA is further enhanced, and the measurable thickness can be further extended from 2nm to 1.8nm, resulting in a very high f_0 of 21.6GHz in W(4)/CoFeB(1.8)/MgO(2.3) /Ta(2) sample. However, the branch of the W(4)/CoFeB(1.8)/MgO(2.3)/Ta(3) sample in Fig. 3.17(d) crosses into a very high resonance field region, which almost reaches the limit that instrument can provide. It will be difficult to detect the signal if the branch shifts toward a higher field region. As a result, the W(4)/CoFeB(2.5)/MgO(2.3)/Ta(3) sample with a branch at optimal resonance field region will be chosen for the W/CoFeB/MgO multilayers system in the next section.

doi:10.6342/NTU202403229

3.4 W/CoFeB/MgO multilayers system

In this section, the structure of the multilayers is shown in Fig 3.19, the Ta(2) in the structure will serve as a space layer between the repeat layers W(4)/CoFeB(t)/MgO(2.3), and a capping layer Ta(3) on the top of the structure is to prevent the structure from oxidation. The repeat layer W(4)/CoFeB(t)/MgO(2.3) will be repeated from 1 to 5 times, and these samples are denoted as $[W(4)/CoFeB(t)/MgO(2.3)]_n$ hereafter, where n is the repetition number. Note that each of the samples will be annealed at 300℃ for 1hr.

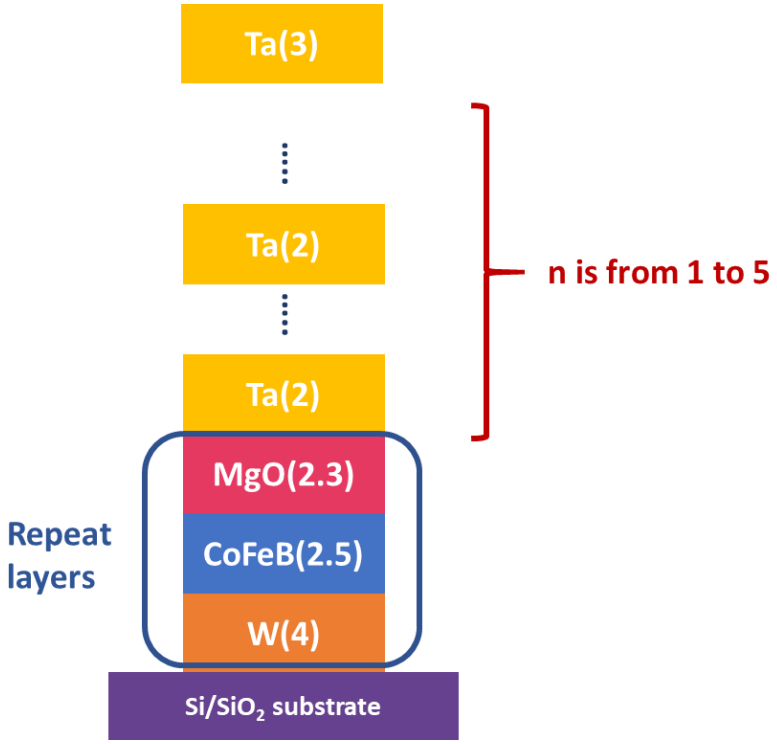

Figure 3.19 The schematic diagram of the samples structure in W/CoFeB/MgO multilayers.

The ST-FMR spectra for each sample are displayed in Fig 3.20. It can be observed that the signal decreases as n increases and can't be detected when n=5. Therefore, the ST-FMR spectra in Fig 3.20 only show the $[W(4)/CoFeB(2.5)/MgO(2.3)]_n$ sample with n=1~4. The resonance field of all samples shifts toward the lower-field region when the frequency increases, which corresponds to the $H_0 < H_a^{FMR}$ condition of a PMA samples.

doi:10.6342/NTU202403229

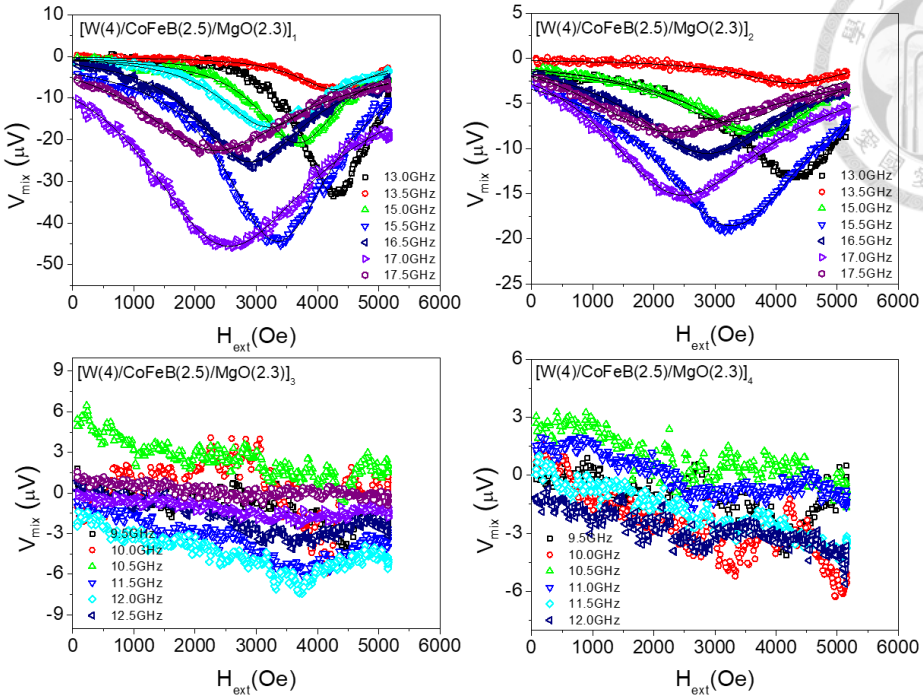

Figure 3.20 ST-FMR spectra with different n for the $[W/CoFeB/MgO]_n$ samples.

The frequency as a function of resonance field, $4\pi M_{eff}$ and f_0 for each sample is shown in Fig 3.21(a), (b) and (c), respectively. In contrast to the previous section, the $[W(4)/CoFeB(t)/MgO(2.3)]_1$ in this section shov (b) ignificantly difference value of $4\pi M_{eff}$. This may related to the different conditions in our sputtering system and causing the thickness discrepancy for the two samples. From Fig 3.21(b), it can be observed that the $4\pi M_{eff}$ decreases as n increases from 2 to 4, indicating the reduction of the PMA strength. Because of the PMA decreases, f_0 decreases from 18 GHz to 14GHz when n increases from 2 to 4. However, it's still a sizable value of f_0 that compares with the Pt/Co/Pt multilayer system. The PMA arises at the CoFeB/MgO interface is strongly depends on the CoFeB/MgO crystallinity and sensitive to the anneling temperature, so the futher analysis on W/CoFeB/MgO multilayer system with different annealing condition can be more discussed in future works to improve the PMA stability.

doi:10.6342/NTU202403229

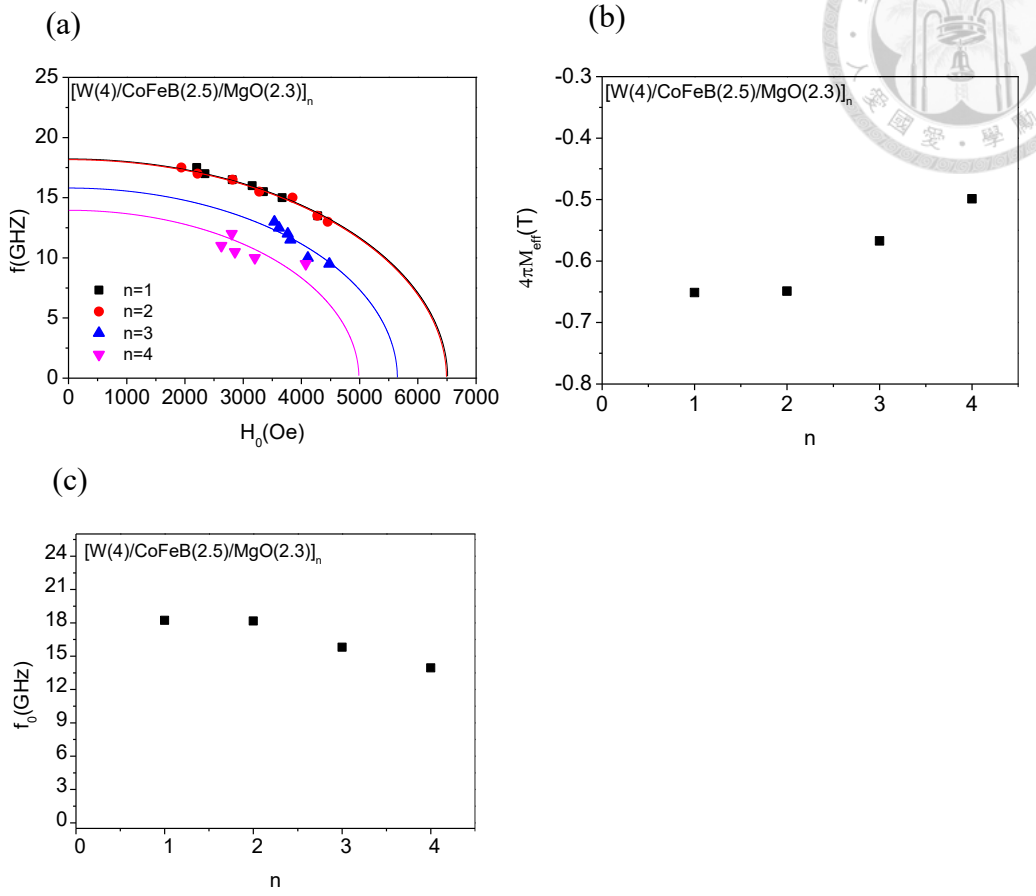

Figure 3.21 (a) Function f as a resonance field H_0, (b) $4\pi M_{eff}$ and (c) f_0 with different n in $[W(4)/CoFeB(2.5)/MgO(2.3)]_n$ samples.

The out-of-plane hysteresis loop and the H_c with different n $[W(4)/CoFeB(2.5)/MgO(2.3)]_n$ is displayed in Fig 3.22 (a) and (b). It can observed that there is a ladder-like hysteresis loop presence in n=3 and 4 samples, which indicates a multiple switching behavior. This may be attributed to the weak exchange coupling between the CoFeB layer due to a large spacer between them, resulting in an incoherent reversal of each CoFeB layer. This ladder-like hysteresis loop is also present in the Co/Pt/Co system when Pt gets thicker in the previous report[75]. However, this phenomenon is not observed in our Pt/Co/Pt multilayer system and may be ascribed to the strong coupling between Co.

doi:10.6342/NTU202403229

This non-coherent reversal of each CoFeB will lead to an increase in H_c, which can be observed in Fig 3.22(b). H_c slightly increases from 23 to 27 Oe when n increases from 1 to 2, and then significantly rises to 90 O when n increases to 4.

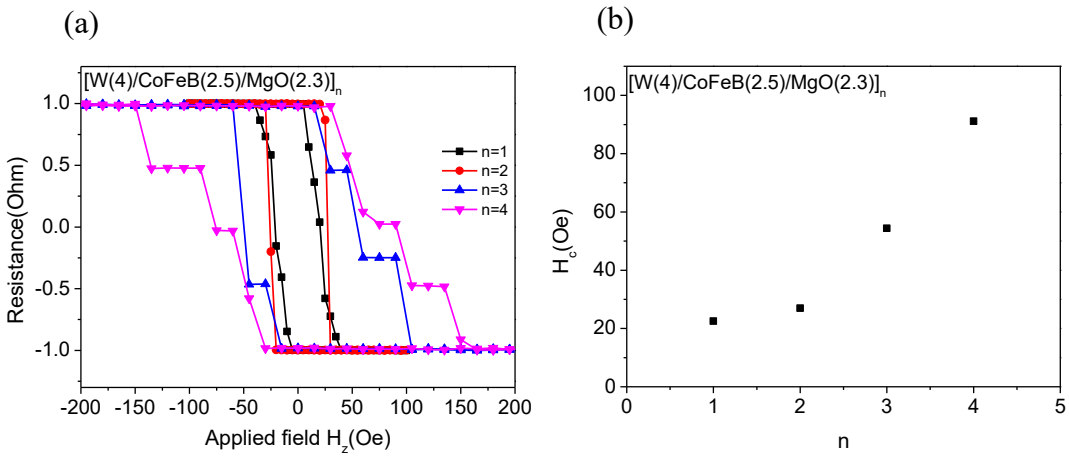

Figure 3.22 The out-of-plane hysteresis loop and (b) the H_c with different n in $[W(4)/CoFeB(2.5)/MgO(2.3)]_n$ samples.

In summary, it can be found that the PMA deteriorates when the repeat layer increases in W/CoFeB/MgO multilayer system, leading to a decrease of f_0. When n increases from 1 to 4, f_0 decreases correspondingly from 18GHz to 14GHz. However, it's still a sizable value compared to the Co/Pt/Co multilayer system. Due to the weak coupling between the CoFeB layer, an incoherent reversal of CoFeB is observed in the hysteresis loop, leading to aa significant increase in H_c from 23 Oe to 90 Oe when n increases from 1 to 4.

doi:10.6342/NTU202403229

3.5 VSM measurement

To confirm that the effective demagnetization field measured by the ST-FMR is reasonable, a series of Pt/Co(t)/Pt and W/CoFeB(t)/MgO samples are prepared by the VSM measurements, where the units in parenthesis is nanometers.

The in-plane Hysteresis loop for Pt(2)/Co(t=4, 4.5, 5, 5.5)/Pt(2) samples with different Co thickness and the saturation magnetization as a function of Co thickness is displayed in Fig 3.23(a) and (b), respectively. We can obtain the value of saturation magnetization M_s and the magnetic dead layer thickness t_{dead} from Fig 3.23 (b) by the equation(3.3) [78], and the obtained value of M_s and the t_{dead} is 1290emu/cc and 0.405nm, respectively.

$$M = M_s(t - t_{dead}) \tag{3.3}$$

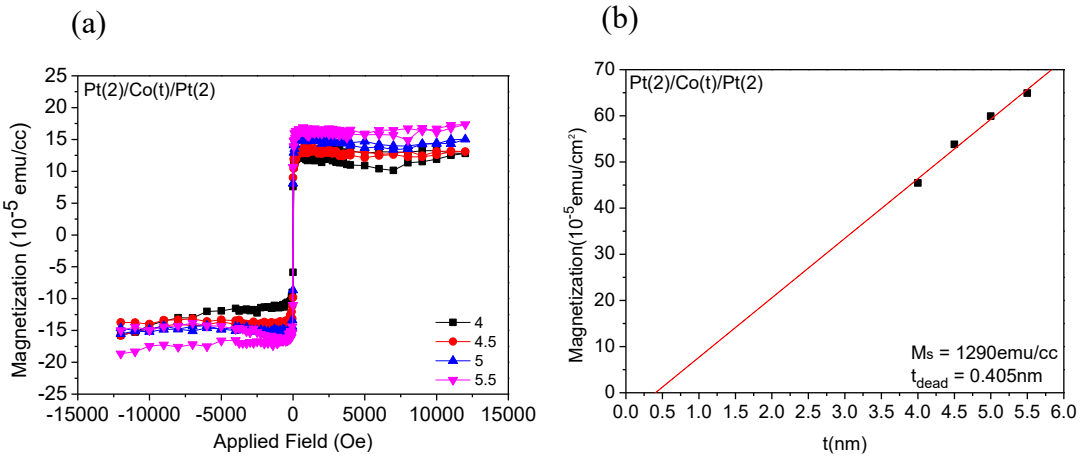

Figure 3.23 (a) In-plane Hysteresis loop for Pt(2)/Co(t)/Pt(2) samples with different Co thickness. (b) Magnetization times Co thickness as a function of Co thickness.

doi:10.6342/NTU202403229

The effective Co thickness t_{eff} times effective anisotropy field K_{eff} as a function of t_{eff} is displayed in Fig 3.6, where $t_{eff} = t - t_{dead}$ and $K_{eff} = H_k M_s/2$. Note that $H_k = -4\pi M_{eff}$. Therefore, the positive K_{eff} is correspond to the sample with the perpendicular anisotropy. On the other hand, the negative K_{eff} is correspond to the sample with in-plane magnetic anisotropy. The K_{eff} can be expressed as[78]

$$K_{eff} = K_v + 2\frac{K_s}{t_{eff}} \tag{3.4}$$

, where K_v is the bulk anisotropy constant and K_s is the interface anisotropy constant. Therefore, we can obtain the value of K_v and K_s from Fig 3.24 by the linear fitting. The obtained value of K_v and K_s is -0.8×10^{-7} erg/cm^3 and 0.46 erg/cm^2. Although there exists a deviation between our results and other reports[75-79], they are still within the same order of magnitude, as displayed in Table 3.1.

Table3.1 List of the obtained value of M_s, K_s and K_v and compared with others reports.

Sample structure	M_s (emu/cc)	K_s (erg/cm^2)	K_v (×10^7 erg/cc)	Ref
Pt(2)/Co(1.2-3.3)/Pt(2)	1290	0.46	-0.8	This work
Co(0.4)/Pt(0.9)	n/a	0.31	-0.8	[79]
Ta(3)/Pt(5)/Co(0.4-3)/Pt(3)	1430	0.9	-1.2	[80]
Pt(1)/Co(0.1-2) Pt(0.5)/Co(0.1-2)	n/a	0.8 0.6	-1.3 -1.58	[81]
Pt(3.4)/Co(0.35-3)/Pt(6.5)	1420	0.7	n/a	[82]
[Co(2.5)/Pt(0.09-1.8)]$_{20}$/Pt(13.5)	1290	0.57	n/a	[83]

doi:10.6342/NTU202403229

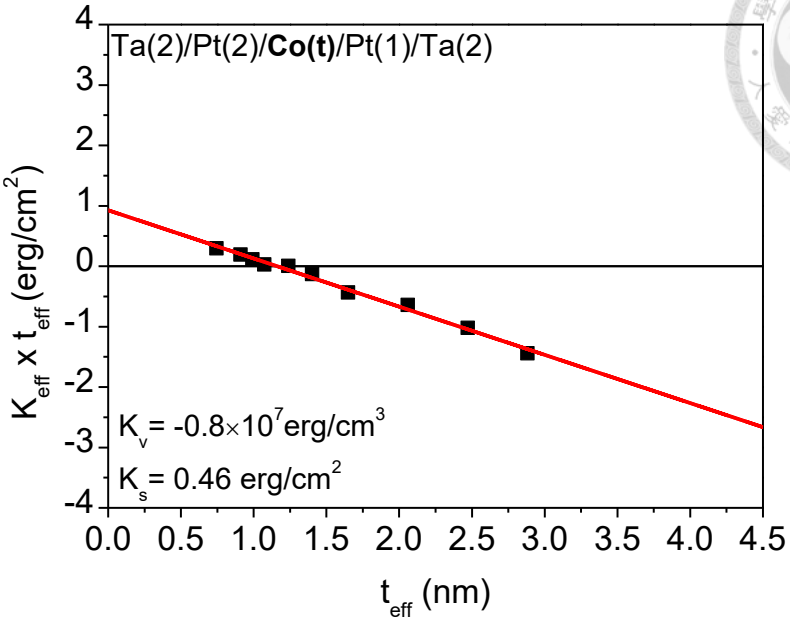

Figure 3.24 $K_{eff} \times t_{eff}$ as a function of t_{eff}.

The in-plane Hysteresis loop for the as-grown and the annealed samples in W/Co(t)/MgO samples with different CoFeB thickness is displayed in Fig 3.25(a), and the saturation magnetization as a function of CoFeB thickness is displayed in Fig 3.25(b). The obtained value of M_s is 566 emu/cc for the as-grown samples and increases to 717 emu/cc after annealing, accompanied by a reduction in the magnetic dead layer. However, the measured value of M_s is significantly smaller than those reported in other studies[84, 85], leading to a considerably smaller value of K_v, while K_s is at the same order of magnitude, as displayed in Table 3.2.

doi:10.6342/NTU202403229

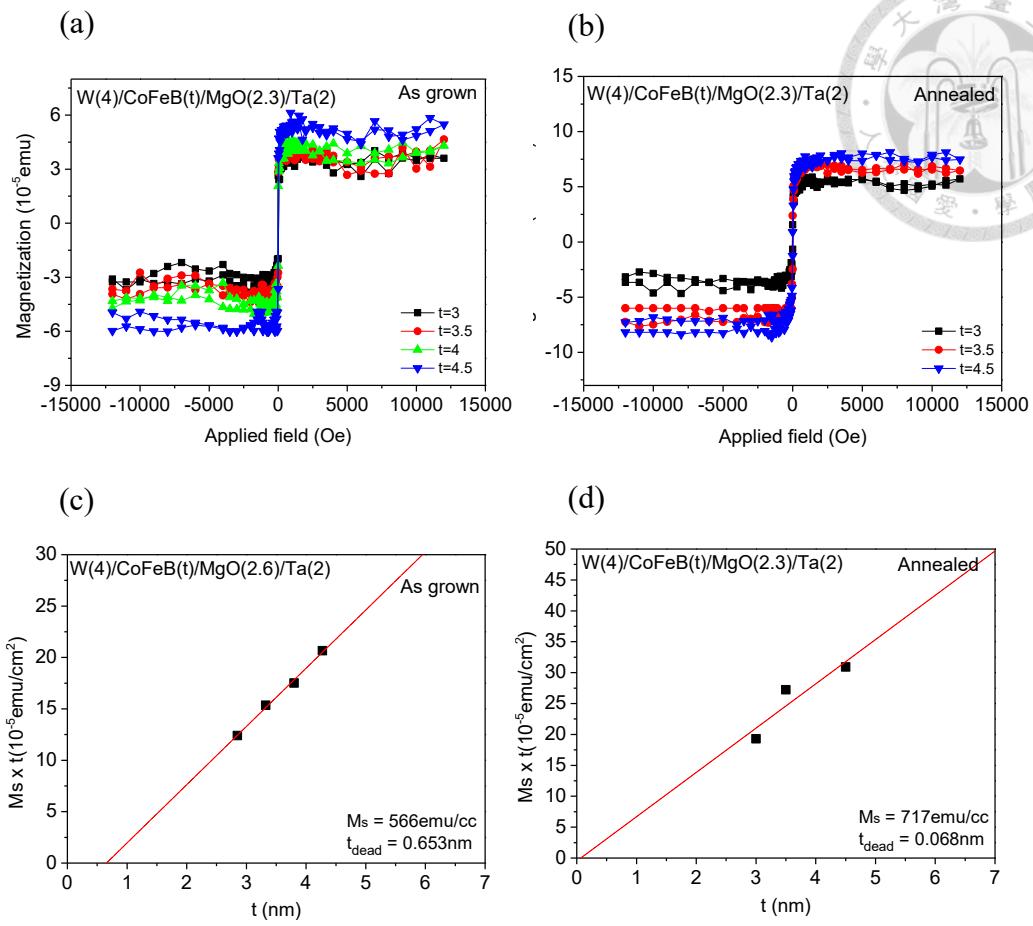

Figure 3.25 In-plane Hysteresis loop for W(4)/CoFeB(t)/MgO(2.3)/Ta((2) with different CoFeB thickness for (a) as grown samples and (b) annealed samples (b) Magnetization times CoFeB thickness as a function of CoFeB thickness.

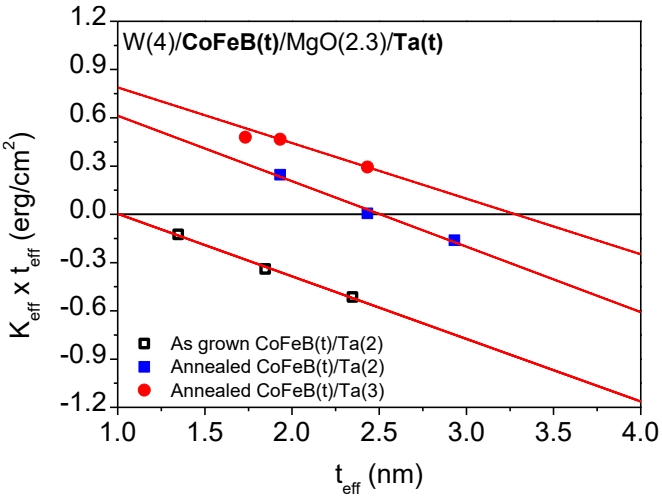

Figure 3.26 The effective CoFeB thickness t_{eff} dependence of $K_{eff} \times t_{eff}$ for as grown samples and annealed samples in W/CoFeB(t)/MgO series

doi:10.6342/NTU202403229

Table 3.1. List of the obtained value of M_s, K_s and K_v and compared with others reports.

Sample structure	M_s (emu/cc)	K_s (erg/cm^2)	K_v (×10^7 erg/cc)	Ref
W(4)/CoFeB(2-3)/MgO/Ta(2) As grown	566	0.2	-0.39	This work
W(4)/CoFeB(2-3)/MgO/Ta(2) Annealed 300℃ 1 hr	717	0.51	-0.41	
W(4)/CoFeB(2-3)/MgO/Ta(3) Annealed 300℃ 1 hr		0.57	-0.35	
W(3)/CoFeB/(0.9-1.5)/MgO(1)/Ta(2) Annealed 300℃ 1 hr	1307	0.7	n/a	[84]
MgO/CoFeB(1.1 - 4)/MgO/Ta(5) Annealed 300℃ 1 hr	1280	0.6	n/a	[85]

doi:10.6342/NTU202403229

Chapter 4 Conclusion

In conclusion, it can be observed that the zero-field ferromagnetic resonance frequency (f_0) can be tilted away from 0 if a sample exhibits a sizable PMA strength. For an inductor used in RF IC applications, it is generally desired for its self-resonance frequency (the frequency at which the inductance drops to 0) to exceed 10 GHz[26]. Therefore, the ferromagnetic resonance frequency of the core material is also often expected to exceed 10 GHz. By modifying the PMA with the ferromagnetic layer thickness t_{FM}, the f_0 is successfully tuned beyond 10 GHz in both Pt/Co/Pt and W/CoFeB/MgO system. The Pt/Co/Pt multilayer system and W/CoFeB/MgO multilayer system with the optimal t_{FM} were also investigated. The f_0 of both multilayer systems decreases when the repetition number >1. For the Pt/Co/Pt multilayer system, the reversed structure samples show a more stable PMA at relatively high repetition numbers compared to the non-reversed structure samples, resulting in a higher f_0 of 3.8 GHz when the repetition number is 5. In addition, the samples with reversed structure also possess a 5∼6 times smaller coercivity than those with non-reversed structure. These better performances in the reversed structure imply that the roughness of the sample may play a role in affecting f_0 and coercivity. For the W/CoFeB/MgO multilayer system, the f_0 still remains around 14GHz when the repetition number comes to 4. However, due to the incoherent reversal of CoFeB layers, the coercivity field significantly increases in the samples with relatively high repetition numbers.

The coercivity field and the f_0 for all the PMA samples are summarized in Fig 4.1. For an ideal core material, we hope the material properties are concentrated in the bottom-right corner of the diagram. Overall, the samples in the W/CoFeB/MgO multilayer system possess a very high f_0 (>14GHz) and a lower coercivity field compared to those in the

doi:10.6342/NTU202403229

Pt/Co/Pt multilayer system. This high level of f_0 demonstrates their potential for high-frequency inductor core material. Moreover, the insulated materials of MgO between the conductive materials can reduce the path of the eddy current to prevent the eddy current loss. However, it still needs a lot of work to reach its full potential. As displayed in Table 4.1, the coercivity field of the samples in the W/CoFeB/MgO multilayer system is still higher compared to other works. Additionally, to substantially enhance the inductance in practical applications, further study on W/CoFeB/MgO multilayer system with higher repetition numbers is needed.

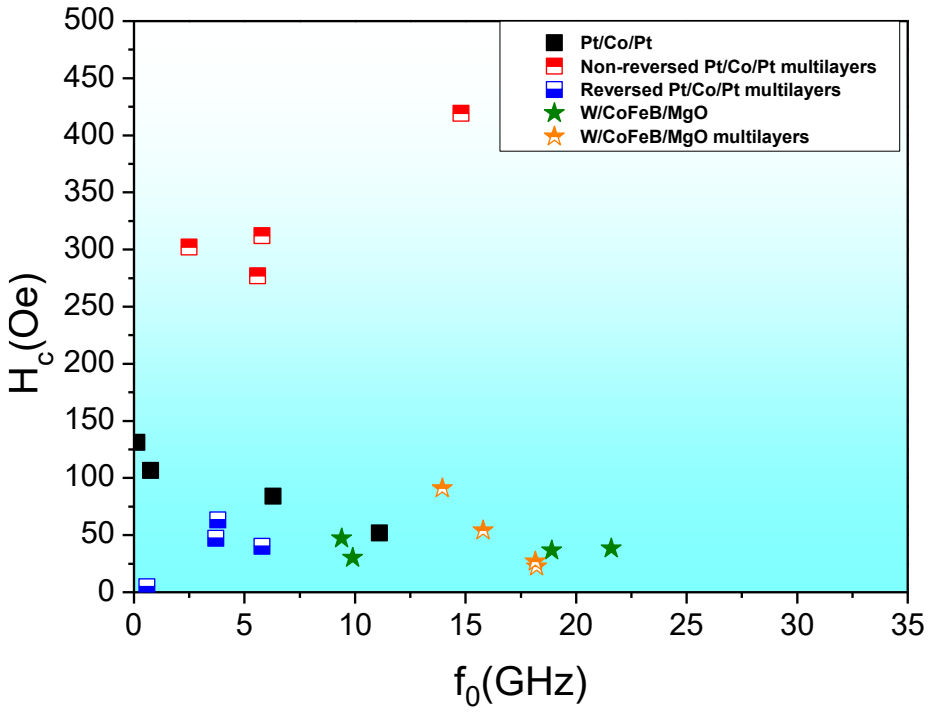

Figure 4.1 A summary of the coercivity and the zero-field ferromagnetic resonance frequency for the PMA samples in Pt/Co/Pt, Pt/Co/Pt multilayers, W/CoFeB/MgO, and W/CoFeB/MgO multilayers system.

doi:10.6342/NTU202403229

Table 4.1 The summary of f_0 and H_c from other works.

Sample structure	Magnetic anisotropy	f_0 (GHz)	H_c(Oe)	Ref
$[W(4)/CoFeB(2.5nm)/MgO(2.3)/Ta]_4$	Perpendicular anisotropy	14	91(easy axis)	This work
Ta(2)/Pt(3)/$[Pt(1)/Co(1)]_5$/Pt(1)/Ta(2)	Perpendicular anisotropy	2.5	302(easy axis)	This work
Ta(2)/Pt(1)/ $[Pt(1)/Co(1)]_5$ /Pt(3)/Ta(2)	Perpendicular anisotropy	3.8	63(easy axis)	This work
$[CoFeB(63nm)/SiO_2(6nm)]_{16}$	In-plane uniaxial anisotropy	3.3	n/a	[38]
$[CoFe(50nm)/IrMn(8nm)]_5$	In-plane uniaxial anisotropy	5.5	n/a	[51]
$[CoNb(11.5nm)/Ta(1.8nm)]_8$	In-plane uniaxial anisotropy	6.5	n/a	[52]
$[CoFeSiO(6nm)/SiO_2(1nm)]_{57}$	In-plane uniaxial anisotropy	2	n/a	[86]
FeCoHfN(100nm)	In-plane uniaxial anisotropy	6.43	~60(easy axis)	[47]
CoZrTaB(250nm)	Perpendicular anisotropy	~1	~16(hard axis)	[87]
FeCoB(500nm)	In-plane uniaxial anisotropy	3.3	1.5(hard axis)	[49]
CoFeB(40nm)	In-plane uniaxial anisotropy	9.7	275(easy axis) ~20(hard axis)	[45]
$FeCoN_x$(60nm)	In-plane uniaxial anisotropy	3.5	~30 (easy axis) ~10(hard axis)	[48]

References

[1] Tang, D.D. and C.-F. Pai, MAGNETIC MEMORY TECHNOLOGY: Spin-transfer-torque Mram and Beyond. 2020: John Wiley & Sons.

[2] Chevalier, A. and M. Le Floc'H, Dynamic permeability in soft magnetic composite materials. Journal of Applied Physics, 2001. **90**(7): p. 3462-3465.

[3] Zhang, R., et al., Current-induced magnetization switching in a CoTb amorphous single layer. Physical Review B, 2020. **101**(21): p. 214418.

[4] González, J.A., J.P. Andrés, and R. López Antón, Applied Trends in Magnetic Rare Earth/Transition Metal Alloys and Multilayers. Sensors, 2021. **21**(16): p. 5615.

[5] Zhao, Z., et al., Spin Hall switching of the magnetization in Ta/TbFeCo structures with bulk perpendicular anisotropy. Applied Physics Letters, 2015. **106**(13).

[6] Liu, Y., et al., Effect of Mo capping layers thickness on the perpendicular magnetic anisotropy in MgO/CoFeB based top magnetic tunnel junction structure. Chinese Physics B, 2016. **25**(11): p. 117805.

[7] An, G.-G., et al., Highly stable perpendicular magnetic anisotropies of CoFeB/MgO frames employing W buffer and capping layers. Acta Materialia, 2015. **87**: p. 259-265.

doi:10.6342/NTU202403229

[8] Carcia, P., Perpendicular magnetic anisotropy in Pd/Co and Pt/Co thin-film layered structures. Journal of applied physics, 1988. **63**(10): p. 5066-5073.

[9] An, Y., et al., Structural and magnetic properties of Pt in Co/Pt multilayers. Applied surface science, 2011. **257**(17): p. 7427-7431.

[10] Chowdhury, P., et al., Effect of coherent to incoherent structural transition on magnetic anisotropy in Co/Pt multilayers. Journal of Applied Physics, 2012. **112**(2).

[11] Kokado, S. and M. Tsunoda, Anisotropic magnetoresistance effect: general expression of AMR ratio and intuitive explanation for sign of AMR ratio. Advanced Materials Research, 2013. **750**: p. 978-982.

[12] Yang, S. and J. Zhang, Current progress of magnetoresistance sensors. Chemosensors, 2021. **9**(8): p. 211.

[13] Velev, J., et al., Ballistic anisotropic magnetoresistance. Physical review letters, 2005. **94**(12): p. 127203.

[14] Fernández-Roldán, J.A., Micromagnetism of cylindrical nanowires with compositional and geometric modulations. 2019.

[15] Wang, H., et al., Scaling of spin Hall angle in 3d, 4d, and 5d metals from Y 3 Fe 5 O 12/metal spin pumping. Physical review letters, 2014. **112**(19): p. 197201.

[16] Emori, S., et al., Current-driven dynamics of chiral ferromagnetic domain walls. Nature materials, 2013. **12**(7): p. 611-616.

[17] Chen, F., et al., Ferromagnetic resonance induced large microwave magnetodielectric effect in cerium doped Y3Fe5O12 ferrites. Scientific reports, 2016. **6**(1): p. 28206.

[18] Coey, J.M., Magnetism and magnetic materials. 2010: Cambridge university press.

[19] Senoy, T. and M. Anantharaman, Fabrication of thin films and nano columnar structures of Fe-Ni amorphous alloys and modification of its surface properties by thermal annealing and swift heavy ion irradiation for tailoring the magnetic properties. 2009, Cochin University of Science & Technology.

[20] Selvaraj, S.L., et al. On-chip thin film inductor for high frequency DC-DC power conversion applications. in *2020 IEEE Applied Power Electronics Conference and Exposition (APEC)*. 2020. IEEE.

doi:10.6342/NTU202403229

[21] Adly, A., Controlling linearity and permeability of iron core inductors using field orientation techniques. IEEE transactions on magnetics, 2001. **37**(4): p. 2891-2893.

[22] Ning, N., et al., A tunable magnetic inductor. IEEE transactions on magnetics, 2006. **42**(5): p. 1585-1590.

[23] Swihart, M.A., Inductor cores–material and shape choices. Magnetics®-www. mag-inc. com, 2004.

[24] Nitta, H., et al., Fabrication and characterization CoZrO films deposited by facing targets reactive sputtering for micro magnetic inductors. IEEE Magnetics Letters, 2023.

[25] Wei, H., et al., Techniques to enhance magnetic permeability in microwave absorbing materials. Applied Materials Today, 2020. **19**: p. 100596.

[26] Hao, W., et al., Advances and Perspectives in Magnetic-Integrated Inductors for RF ICs. IEEE Transactions on Materials for Electron Devices, 2024.

[27] El-Ghazaly, A., R. White, and S. Wang. Thin-Film Magnetic Inductors for Gigahertz Integrated Applications. in *2018 IEEE International Magnetics Conference (INTERMAG)*. 2018. IEEE.

[28] Acher, O. and A. Adenot, Bounds on the dynamic properties of magnetic materials. Physical review B, 2000. **62**(17): p. 11324.

[29] Yamada, S. and E. Otsuki, Analysis of eddy current loss in Mn–Zn ferrites for power supplies. Journal of applied physics, 1997. **81**(8): p. 4791-4793.

[30] Cheng, Z., et al. Hysteresis loss analysis based on W/sub h/-B/sub m/function. in *The Fourth International Conference on Computation in Electromagnetics, 2002. CEM 2002 (Ref. No. 2002/063)*. 2002. IET.

[31] Bermúdez, A., D. Gómez, and P. Salgado, Eddy-current losses in laminated cores and the computation of an equivalent conductivity. IEEE Transactions on magnetics, 2008. **44**(12): p. 4730-4738.

[32] Lamprecht, E., M. Hömme, and T. Albrecht. Investigations of eddy current losses in laminated cores due to the impact of various stacking processes. in *2012 2nd International Electric Drives Production Conference (EDPC)*. 2012. IEEE.

[33] Zhao, G., C. Wu, and M. Yan, Fe-Based Soft Magnetic Composites With High Bs and Low Core Loss by Acidic Bluing Coating. IEEE Transactions on Magnetics, 2015. **51**(11): p. 1-4.

doi:10.6342/NTU202403229

[34] Luo, F., et al., Ultra-low inter-particle eddy current loss of Fe3Si/Al2O3 soft magnetic composites evolved from FeSiAl/Fe3O4 core-shell particles. Journal of Magnetism and Magnetic Materials, 2019. **484**: p. 218-224.

[35] Moutassem, W. and G.J. Anders, Calculation of the eddy current and hysteresis losses in sheathed cables inside a steel pipe. IEEE Transactions on Power Delivery, 2010. **25**(4): p. 2054-2063.

[36] Tan, F.D., J.L. Vollin, and S.M. Cuk, A practical approach for magnetic core-loss characterization. IEEE Transactions on Power Electronics, 1995. **10**(2): p. 124-130.

[37] Gorecki, K. and K. Detka, Improved method for measuring power losses in the inductor core. IEEE Transactions on Instrumentation and Measurement, 2020. **70**: p. 1-10.

[38] El-Ghazaly, A., R.M. White, and S.X. Wang, GHz-Band Integrated Magnetic Inductors. arXiv preprint arXiv:1702.03009, 2017.

[39] Yang, J.-T., et al. A CMOS radio frequency receiver for bluetooth applications. in *2009 1st Asia Symposium on Quality Electronic Design*. 2009. IEEE.

[40] Lee, S., et al., Dual-band circularly polarized annular slot antenna with a lumped inductor for GPS application. IEEE Transactions on Antennas and Propagation, 2020. **68**(12): p. 8197-8202.

[41] Zhao, X., et al., Voltage control of ferromagnetic resonance and spin waves. Chinese Physics B, 2018. **27**(9): p. 097505.

[42] Perrin, G., J. Peuzin, and O. Acher, Control of the resonance frequency of soft ferromagnetic amorphous thin films by strip patterning. Journal of applied physics, 1997. **81**(8): p. 5166-5168.

[43] Kim, K.H., M. Yamaguchi, and J. Kim, Ferromagnetic resonance behaviors of integrated CoPdAIO magnetic film on coplanar waveguide. Journal of the Korean Physical Society, 2007. **51**(6): p. 2026-2030.

[44] Das, R., et al., Enhanced soft magnetic properties in N-doped amorphous FeCo thin film. IEEE Transactions on Magnetics, 2023.

[45] Li, C., et al., Tunable zero-field ferromagnetic resonance frequency from S to X band in oblique deposited CoFeB thin films. Scientific reports, 2015. **5**(1): p. 17023.

doi:10.6342/NTU202403229

[46] Chai, G., N.N. Phuoc, and C.K. Ong, Angular tunable zero-field ferromagnetic resonance frequency in oblique sputtered CoFeBSm thin films. Applied Physics Express, 2014. **7**(6): p. 063001.

[47] Phuoc, N.N. and C. Ong, FeCoHfN thin films fabricated by co-sputtering with high resonance frequency. Journal of alloys and compounds, 2011. **509**(9): p. 4010-4013.

[48] Li, T., et al., Microstructure and magnetic properties of FeCoHfN thin films deposited by DC reactive sputtering. Journal of Magnetism and Magnetic Materials, 2022. **547**: p. 168777.

[49] Klemmer, T., et al., Ultrahigh frequency permeability of sputtered Fe–Co–B thin films. Journal of Applied Physics, 2000. **87**(2): p. 830-833.

[50] Das, R., et al., Enhanced soft magnetic properties in N-doped amorphous FeCo thin film. IEEE Transactions on Magnetics, 2023. **59**(11): p. 1-5.

[51] Jiang, R.-F., et al., Exchange-coupled IrMn/CoFe mulitlayers for RF-integrated inductors. IEEE transactions on magnetics, 2007. **43**(10): p. 3930-3932.

[52] Chai, G., et al., Adjust the resonance frequency of (Co90Nb10/Ta) n multilayers from 1.4 to 6.5 GHz by controlling the thickness of Ta interlayers. Applied Physics Letters, 2010. **96**(1).

[53] He, C., et al., Spin-Torque Ferromagnetic Resonance in W/Co− Fe− B/W/Co− Fe− B/Mg O Stacks. Physical Review Applied, 2018. **10**(3): p. 034067.

[54] He, C., et al., Spin-torque ferromagnetic resonance measurements utilizing spin Hall magnetoresistance in W/Co40Fe40B20/MgO structures. Applied Physics Letters, 2016. **109**(20).

[55] Satake, M., et al., Correlation between dry etching resistance of Ta masks and the oxidation states of the surface oxide layers. Journal of Vacuum Science & Technology B, 2015. **33**(5).

[56] Nagaosa, N., et al., Anomalous hall effect. Reviews of modern physics, 2010. **82**(2): p. 1539-1592.

[57] Venkateshvaran, D., et al., Anomalous Hall effect in magnetite: Universal scaling relation between Hall and longitudinal conductivity in low-conductivity ferromagnets. Physical Review B—Condensed Matter and Materials Physics, 2008. **78**(9): p. 092405.

doi:10.6342/NTU202403229

[58] Wang, J., et al., Anomalous Hall effect and magnetoresistance of (FexSn1− x) 1− y (SiO2) y films. Journal of Physics D: Applied Physics, 2007. **40**(8): p. 2425.

[59] Hirsch, J., Spin hall effect. Physical review letters, 1999. **83**(9): p. 1834.

[60] Harder, M., et al., Analysis of the line shape of electrically detected ferromagnetic resonance. Physical Review B, 2011. **84**(5): p. 054423.

[61] Zhang, W., Charge to Spin Current Efficiency Studied by Spin Torque Ferromagnetic Resonance in Various Metal Heterostructures. 2015: Stanford University.

[62] Wang, Y., R. Ramaswamy, and H. Yang, FMR-related phenomena in spintronic devices. Journal of Physics D: Applied Physics, 2018. **51**(27): p. 273002.

[63] Liu, L., et al., Spin-torque ferromagnetic resonance induced by the spin Hall effect. Physical review letters, 2011. **106**(3): p. 036601.

[64] Bangar, H., et al., Optimization of growth of large-area SnS thin films and heterostructures for spin pumping and spin-orbit torque. Physical Review Materials, 2023. **7**(9): p. 094406.

[65] Shu, X., et al., Role of interfacial orbital hybridization in spin-orbit-torque generation in Pt-based heterostructures. Physical Review Applied, 2020. **14**(5): p. 054056.

[66] He, C., et al., Spin-Torque Ferromagnetic Resonance in W/Co-Fe-B/W/Co-Fe-B/Mg O Stacks. Physical Review Applied, 2018. **10**(3): p. 034067.

[67] Mizukami, S.M.S., Y.A.Y. Ando, and T.M.T. Miyazaki, The study on ferromagnetic resonance linewidth for NM/80NiFe/NM (NM= Cu, Ta, Pd and Pt) films. Japanese journal of applied physics, 2001. **40**(2R): p. 580.

[68] Tokaç, M., et al., Interfacial contribution to thickness dependent in-plane anisotropic magnetoresistance. AIP Advances, 2015. **5**(12).

[69] Kobs, A., et al., Anisotropic interface magnetoresistance in Pt/Co/Pt sandwiches. Physical review letters, 2011. **106**(21): p. 217207.

[70] Qiu, J., et al., Effect of roughness on perpendicular magnetic anisotropy in (Co90Fe10/Pt) n superlattices. Aip Advances, 2016. **6**(5).

[71] Lee, T., et al., Strength of perpendicular magnetic anisotropy at bottom and top interfaces in [Pt/Co/Pt] trilayers. IEEE Magnetics Letters, 2014. **5**: p. 1-4.

doi:10.6342/NTU202403229

[72] Won, Y.C. and S.H. Lim, Interfacial properties of [Pt/Co/Pt] trilayers probed through magnetometry. Scientific reports, 2021. **11**(1): p. 10779.

[73] Wang, X., et al., Effect of the repeat number and Co layer thickness on the magnetization reversal process in [Pt/Co (x)] N multilayers. Journal of Physics D: Applied Physics, 2020. **53**(21): p. 215001.

[74] Liu, Y., et al., Strong perpendicular magnetic anisotropy in [Co/Pt] n ultrathin superlattices. Applied Physics Express, 2016. **10**(1): p. 013005.

[75] Wang, K., et al., Optimization of Co/Pt multilayers for applications of current-driven domain wall propagation. Journal of applied physics, 2011. **110**(8).

[76] Zhao, Y.-P., et al., Effect of surface roughness on magnetic domain wall thickness, domain size, and coercivity. Journal of Applied Physics, 2001. **89**(2): p. 1325-1330.

[77] Qu, D., et al., Self-consistent determination of spin Hall angles in selected 5 d metals by thermal spin injection. Physical Review B, 2014. **89**(14): p. 140407.

[78] Gabor, M.S., C. Tiusan, and T. Petrisor, The influence of the capping layer on the perpendicular magnetic anisotropy in permalloy thin films. IEEE Transactions on Magnetics, 2014. **50**(11): p. 1-4.

[79] Hashimoto, S., Y. Ochiai, and K. Aso, Perpendicular magnetic anisotropy and magnetostriction of sputtered Co/Pd and Co/Pt multilayered films. Journal of applied physics, 1989. **66**(10): p. 4909-4916.

[80] Bandiera, S., et al., Asymmetric interfacial perpendicular magnetic anisotropy in Pt/Co/Pt trilayers. IEEE Magnetics Letters, 2011. **2**: p. 3000504-3000504.

[81] Guo, V.W., et al., A survey of anisotropy measurement techniques and study of thickness effect on interfacial and volume anisotropies in Co ／ Pt multilayer media. Journal of Applied Physics, 2006. **99**(8).

[82] Kisielewski, M., et al., Magnetic anisotropy and magnetization reversal processes in Pt/Co/Pt films. Journal of magnetism and magnetic materials, 2003. **260**(1-2): p. 231-243.

[83] Zhang, Z., P. Wigen, and S. Parkin, Pt layer thickness dependence of magnetic properties in Co/Pt multilayers. Journal of applied physics, 1991. **69**(8): p. 5649-5651.

[84] Kim, G.W., et al., Role of the Heavy Metal's Crystal Phase in Oscillations of Perpendicular Magnetic Anisotropy and the Interfacial Dzyaloshinskii-Moriya Interaction in W/Co-Fe-B/MgO Films. Physical Review Applied, 2018. 9(6):

doi:10.6342/NTU202403229

p. 064005.

[85] Liu, T., J. Cai, and L. Sun, Large enhanced perpendicular magnetic anisotropy in CoFeB/MgO system with the typical Ta buffer replaced by an Hf layer. Aip Advances, 2012. **2**(3).

[86] Ikeda, K., et al., Thin-film inductor for gigahertz band with CoFeSiO-SiO/sub 2/multilayer granular films and its application for power amplifier module. IEEE transactions on magnetics, 2003. **39**(5): p. 3057-3061.

[87] Lordan, D., et al., Origin of perpendicular magnetic anisotropy in amorphous thin films. Scientific Reports, 2021. **11**(1): p. 3734.

doi:10.6342/NTU202403229